Temporal evolution of magma and crystal mush storage conditions in the Bárðarbunga-Veiðivötn volcanic system, Iceland

DOI:
10.1016/j.lithos.2019.105234

Temporal evolution of magma and crystal mush storage conditions in the Bárðarbunga-Veiðivötn volcanic system, Iceland

Alberto Caracciolo[1,2], Enikő Bali[1,2], Guðmundur H. Guðfinnsson[1], Maren Kahl[3], Sæmundur A. Halldórsson[1], Margaret E. Hartley[4], Haraldur Gunnarsson[1]

(1) Nordic Volcanological Center, Institute of Earth Sciences, University of Iceland, Sturlugata 7, 101 Reykjavík, Iceland.
(2) Faculty of Earth Sciences, University of Iceland, Sturlugata 7, 101 Reykjavík, Iceland.
(3) Institut für Geowissenschaften, Universität Heidelberg, Heidelberg, Germany
(4) School of Earth and Environmental Sciences, University of Manchester, Manchester, UK

*Corresponding author

Alberto Caracciolo
Tel. +354 7794573
Email: alc10@hi.is

Keywords: Iceland; Crystal Mush; Melt Inclusions; Bárðarbunga-Veiðivötn; Thermobarometry; Geochemistry

1. Introduction

For more than 100 years, the concept of a melt-dominated and long-lived magma chamber has been a commonly accepted paradigm in volcanology. However, our understanding of volcanic plumbing systems and processes has improved in the last few decades due to new geophysical, petrological and geological evidence (e.g., Ryan, 2018; Sinton and Detrick, 1992; West et al., 2001). Magma plumbing systems beneath active volcanoes are now envisaged to be characterized by sets of crustal reservoirs that are dominated by relatively liquid-poor crystal mushes (Edmonds et al., 2019; Marsh, 2006). Crystal mushes are dynamic horizons made of a semi-rigid framework of crystals within which the melt is distributed (Cashman et al., 2017; Maclennan, 2019). These bodies cannot be erupted in their entirety due to their rheological properties, but mush fragments can be disaggregated from the system by an ascending melt, and carried to the surface as glomerocrysts, nodules or macrocrysts (Cashman et al., 2017). Evidence from mush fragments is essential to constrain pressure (P), temperature (T), composition (X) and processes operating within a plumbing system.

Magmas in Iceland commonly carry disaggregated fragments of crystal mushes (Cooper et al., 2016; Halldórsson et al., 2018; Hansen and Grönvold, 2000; Neave et al., 2013, 2014, 2017; Óskarsson et al., 2017; Passmore et al., 2012; Svavarsdóttir et al., 2017). Petrological investigations of the geochemical relationship between macrocrysts and their carrier liquids have revealed that some mush fragments are related to their carrier liquid (Neave et al., 2013), while others cannot be cogenetic (Halldórsson et al., 2008). Identifying the location of a magma storage reservoir(s) within a plumbing system and tracking its evolution with time is important for clarifying the functioning of a volcanic system and for future eruption mitigation.

The Bárðarbunga-Veiðivötn volcanic system, located in the Eastern Volcanic Zone (EVZ), is ideal for investigating the temporal and compositional evolution of a basaltic magma storage reservoir(s) on the scale of a single volcanic system. This is because (1) it is one of the most active volcanic systems in Iceland during the Holocene; (2) extrusives consist of phyric and ultra-phyric rocks containing disaggregated crystal mush fragments (e.g., Halldórsson et al., 2018, 2008; Hansen and Grönvold, 2000; Holness et al., 2019); and (3) Holocene tephras from the Bárðarbunga system (Óladóttir et al., 2011) exhibit distinctive compositional variations as a function of time (Fig. 1). Furthermore, a fundamental observation from the Icelandic rift system is the apparent effect of deglaciation on magma plumbing dynamics. This is well documented in the Reykjanes Peninsula (Gee et al., 1998; Jakobsson et al., 1978), in the Western Volcanic Zone (Eason et al., 2015; Sinton et al., 2005) and in the Northern Volcanic Zone (Maclennan et al., 2002; Slater et al., 1998), although it remains unclear if and how magmatic plumbing systems were affected in the EVZ.

In this work, we present mineral, groundmass glass and melt inclusion major and minor elemental compositions from a temporally diverse (fully subglacial to historical) sample set from the Bárðarbunga-Veiðivötn volcanic system in central Iceland. Each sample provides a snapshot of the physical and chemical state of the volcanic system at the time of eruption. By linking geochemical and petrological data with geothermobarometry calculations, we explore the temporal evolution of magma storage conditions in the Bárðarbunga-Veiðivötn system. We first chemically characterize a sample suite comprising fresh nodules, macrocrysts and glass. Secondly, we employ a range of mineral-melt and melt-based thermobarometers (Hartley et al., 2018; Neave et al., 2017; Putirka, 2008; Yang et al., 1996) to evaluate magma storage conditions for each eruptive unit. On the basis of these observations, we make an attempt to reconstruct the architecture of the Bárðarbunga-Veiðivötn magmatic system and the changes occurring within it from the last glacial period to recent times.

2. GEOLOGICAL SETTING AND SAMPLING

2.1 The Bárðarbunga-Veiðivötn volcanic system

The Bárðarbunga volcanic system (Fig. 2) is the most extensive volcanic system in Iceland with a total length of 190 km and an area of about 2500 km^2 (Thordarson and Höskuldsson, 2008). With one eruption every 50 years in the last 1100 years, the Bárðarbunga volcanic system is one of the most active system in Iceland (Larsen and Guðmundsson, 2014). The central edifice is split into two subglacial volcanoes: Bárðarbunga, a ~2009 m-high caldera-bearing volcano situated under the Vatnajökull ice cap, and Hamarinn, a smaller second central volcano located 20 km SW of Bárðarbunga. The associated fissure swarm is commonly subdivided into two segments: the Dyngjuháls fissure swarm extends 55 km north-northeast from Bárðarbunga into the Northern Volcanic Zone, while the Veiðivötn fissure swarm extends 115 km southwest from Bárðarbunga into the Eastern Volcanic Zone.

The southwest part of the Bárðarbunga volcanic system is commonly referred to as the Bárðarbunga-Veiðivötn volcanic system. The Veiðivötn part consists of numerous well-developed volcanic fissures orientated N45° (Larsen, 1984; Larsen and Guðmundsson, 2014; Thordarson and Larsen, 2007). In the extreme southwest, the Veiðivötn fissure swarm propagates into the Torfajökull volcanic system with production of both silicic and mixed products (Larsen, 1984; Mørk, 1984; Zellmer et al., 2008). The latest eruption took place on the northern fissure swarm, producing the 2014-15 Holuhraun lava (Pedersen et al., 2017).

2.2 Sample description

We have selected a suite of geologically well-characterised eruptive units from volcanic formations situated in the Bárðarbunga-Veiðivötn volcanic system (Fig. 2 and Table 1).

Ljósufjöll (Lj)

Ljósufjöll, a subglacial volcanic ridge located within the Veiðivötn fissure system (Lj, Fig. 2). Studied samples are from a glassy pillow lava, corresponding to Ljósufjöll formations b and c (lja and ljb) described by Vilmundardóttir et al. (2000). Ljósufjöll is thought to have erupted early during the last glacial period (Weichselian) and is therefore likely to be younger than 100 ka (Jóhannesson et al., 1982). No prior petrochemical studies have been carried out on Ljósufjöll.

Brandur (B), Fontur (F) and Saxi (S)

Brandur, Fontur and Saxi are three early-Holocene tephra cones located to the east of Þórisvatn lake (B, F, S, Fig. 2). Saxi and Fontur are aligned along a ~2.5 km-long linear fissure, while Brandur is located 3 km west of the fissure on the edge of Þórisvatn lake. The craters consist of unconsolidated, crystal-rich, fine-grained glassy material with plagioclase macrocrysts up to 4 cm long, and abundant nodules of plagioclase, olivine and clinopyroxene (Halldórsson et al., 2008; Hansen and Grönvold, 2000; Holness et al., 2007, 2019; Vilmundardóttir, 1977). These craters have been suggested to be the source of the Þjórsárhraun lava (8.6 ka, e.g. Halldórsson et al., 2008; Hansen and Grönvold, 2000; Hjartarson, 1988; Jakobsson, 1979). In addition to samples collected for this study, we also collected data from samples previously studied by Hansen and Grönvold (2000).

Þjórsárdalshraun (Th) and Drekahraun (Dr) (Tungnaá lava)

Lava flows produced in the Veiðivötn fissure over the last 9 ka, but before the settlement of Iceland in 874 AD, are collectively referred to as the Tungnaá lava sequence. At 45 km^3, this is one of the most voluminous lava sequences in Iceland (Vilmundardóttir, 1977). The source vents of the Tungnaá lavas are now mostly buried by younger formations but were probably located in the southern part of the Veiðivötn fissure swarm (Pinton et al., 2018). Þjórsárdalshraun and Drekahraun (Th and Dr, Fig. 2) are mid-Holocene lavas belonging to the Tungnaá sequence. They are dated to between 3-4 ka BP by tephrochronology (Pinton et al. 2018). Drekahraun samples consist of fresh and vesicular scoria collected west of Drekavatn, near the lava source vents (Dr, Fig. 2). The Þjórsárdalshraun lava was largely emplaced to the north of Hekla volcano, flowing westward following the Þjórsá river and ultimately forming a field of rootless cones in Þjórsárdalur valley (Th, Fig. 2).

Veiðivötn 1477 (V)

The 1477 AD Veiðivötn eruption is the most recent eruption covered by our sample suite. The eruption is considered to be the largest basaltic explosive eruption that has occurred in Iceland in the last 1200 years (Thordarson and Larsen, 2007). It took place on a 65 km long fissure and produced 5-10 km^3 of highly fragmented basaltic tephra and small lava flows. This volume includes both tephras and lavas ranging from basalt to rhyolite which erupted simultaneously as the Veiðivötn magmas entered the Torfajökull silicic center to southwest (McGarvie, 1984; Mørk, 1984; Zellmer et al., 2008). Tephra from this eruption covered an area of 53 km^2 on land and has been found as far afield as Ireland and Sweden (Larsen, 1984; Larsen and Guðmundsson, 2014). Here we study fresh and glassy basaltic scoria from the central and southern part of the main fissure specifically avoiding the mixed magmas near Torfajökull (V1477, Fig. 2).

3. METHODS

3.1 Sample preparation, analytical and thermobarometry methods

Thin sections of well-preserved and representative whole rock samples were made from each unit. Plagioclase, olivine and clinopyroxene crystals (0.5-2.4 mm) were hand-picked from crushed samples, mounted in epoxy resin and polished to expose glassy melt inclusions (MIs). Crystals containing devitrified MIs were heated in a high-temperature furnace at 1210 ± 5 °C, which was expected to exceed the crystallization temperature. The re-homogenized MIs were later exposed at the surface. Major element compositions of macrocrysts (n = 1530), their host glass (n = 328) and olivine- and plagioclase-hosted MIs (n= 436) were determined by electron microprobe (EPMA) using a JEOL JXA-8230 SuperProbe at the University of Iceland. 1σ errors reported in this work are based on multiple standard analyses collected during different analytical sessions. All melt inclusion compositions have been corrected for the effect of post-entrapment crystallization (PEC) on the inclusion walls.

We calculated magma storage temperatures based on glass compositions (Yang et al., 1996) and mineral-glass pairs (Putirka, 2008). Crystallization pressures were calculated based on clinopyroxene-melt pairs, following the method described by Neave and Putirka (2017), which has a standard error of estimate (SEE) of ±1.4 kbar, whereas the olivine-plagioclase-augite-melt (OPAM) barometer (Hartley et al., 2018; Yang et al., 1996) was applied to estimate groundmass glass and MI equilibration pressures (SEE=±1.3 kbar). Full details of analytical methods, homogenization experiments, PEC corrections and thermobarometry calculations are provided as supplementary material (S1).

4. Results

4.1 Petrography

All our samples contain three main macrocryst (>500 µm) phases: olivine, clinopyroxene and plagioclase. Minerals are present either as single grains scattered in the groundmass or in polymineralic glomerocrysts (Fig. 3). Plagioclase is the most common mineral phase in all samples (Fig. 3a). Plagioclase macrocrysts are generally euhedral and range from 500-6000 µm in size, although crystals up to 3-4 cm are found in Brandur, Fontur and Saxi samples. Clinopyroxene macrocrysts range between 500-1600 µm and often occur in glomerocrysts (Fig. 3b), although large euhedral clinopyroxene is occasionally found (Fig. 3c). Olivine macrocrysts are typically 500-2000 µm in size and are either euhedral or show rounded and resorbed habits (Fig. 3d-e). Cr-rich spinel is sporadically found in the groundmass glass and is also widespread as inclusions in olivine and plagioclase macrocrysts.

Naturally quenched melt inclusions are abundant in olivines and plagioclases from Ljósufjöll, Brandur, Fontur, Saxi, and Veiðivötn 1477. The melt inclusions range in size from 10-150 µm (Fig. 3d-e). Plagioclase and olivine crystals from Þjórsárdalshraun and Drekahraun contain MIs that are partially crystallized. Crystals in the tephra cones Brandur, Fontur and Saxi are surrounded by a glassy to fine-grained matrix. Ljósufjöll samples display a coarse-grained groundmass (Fig. 3g) composed of plagioclase, clinopyroxene, olivine and oxides, changing to a cryptocrystalline and glassy matrix towards the pillow margins (Fig. 3h). Drekahraun and Veiðivötn 1477 samples contain a fine-grained matrix with glassy portions at the tephra clast rims. Þjórsárdalshraun samples have a holocrystalline groundmass.

Samples from all localities have plagioclase macrocrysts with cores exhibiting complex internal textures. The inner part is either oscillatory or patchy zoned and always wrapped by euhedral to subhedral rims. The thickness of Ljósufjöll plagioclase rims appears to be correlated with the matrix texture (Fig. 3g-h). Plagioclase rims in contact with coarse-grained groundmass are thicker (~30-70 µm) (Fig. 3g), while plagioclase rims scattered in cryptocrystalline to glassy matrix are thinner (~10-40 µm) (Fig. 3h). Þjórsárdalshraun plagioclase macrocrysts are normally zoned.

In backscattered electron (BSE) images, clinopyroxenes display bright and dark sectors (Fig. 3b). The clinopyroxenes are found either as glomerophyric clots or as fine to coarse intergrowths of clinopyroxene and plagioclase forming next to plagioclase macrocrysts. In Veiðivötn 1477, Ljósufjöll and the tephra cone samples, clinopyroxene also occurs as scattered single grains (Fig. 3c). Olivine crystals are often resorbed, especially in Brandur, Fontur and Saxi samples, although euhedral crystals are found in all localities.

Abundant cm-size (up to 10 cm) olivine gabbro xenoliths are found in the Brandur, Fontur and Saxi cones (Fig. 3e). The five studied nodules all contain 70-80 vol.% plagioclase in a subophitic texture with some resorbed interstitial olivine and clinopyroxene. The framework is sustained by transparent, light brown interstitial glass, which is locally crystallized to a fine intergrowth of plagioclase, clinopyroxene ± olivine (see also Hansen and Grönvold, 2000 and Holness et al., 2007). Two xenoliths, 0.5-0.9 cm in size, were also found in the Þjórsárdalshraun lava samples (Fig. 3f). They consist of olivine-free gabbro, with plagioclase and clinopyroxene forming an ophitic texture, and contain localized pockets of coarse- to fine-grained interstitial material (Fig. 3f).

4.2 Mineral and glass chemistry

Macrocryst compositions are summarized in Fig. 4a-c. For each mineral phase, variation diagrams are also shown in Fig. 4d-f and in the supplementary material (Fig. S1.2-S1.4). Groundmass glass and melt inclusion compositions are reported in Fig. 1 and Fig. 5. The full EPMA dataset is provided as supplementary material (S2).

4.1 Plagioclase

Plagioclase macrocrysts commonly have bytownitic to anorthitic compositions. Ljósufjöll plagioclase macrocryst cores display a narrow compositional range of $An_{86-90.5}$, whereas the composition of the rims depends on the groundmass glass texture (Fig. 3g-h). Plagioclase rims in contact with coarse-grained groundmass have more evolved compositions within the range An_{65-71}, while plagioclase rims adjacent to cryptocrystalline to glassy groundmass record compositions within the range An_{79-86} (Fig. 4a and 3d). Plagioclase macrocryst cores from Brandur, Fontur and Saxi samples are in the range $An_{83-91.5,}$ with Fontur plagioclase cores having slightly less compositional variation of $An_{86-90.5}$ (Fig. 4a). All plagioclase macrocrysts are surrounded by An_{71-81} rims. Þjórsárdalshraun and Drekahraun plagioclase macrocryst core and rim compositions are between An_{84-91} and An_{71-86}, respectively (Fig. 4a and 4d), while plagioclases found in Þjórsárdalshraun nodules are more homogeneous ($An_{85-89.5}$). Macrocryst cores and rims from Veiðivötn 1477 display the largest compositional variation of all studied localities. Plagioclase core compositions are An_{78-91}, while rims are An_{66-77}.

4.2 Clinopyroxene

Clinopyroxenes have augititic compositions. Ljósufjöll clinopyroxene cores and dark sectors in BSE images have compositions of Mg# 84-87 (Mg#=[(MgO_{mol})/(MgO_{mol}+FeO^{tot}_{mol})]*100), while rims and bright sectors have Mg# 76-86 (Fig. 4b and 3e). Brandur, Fontur and Saxi cones contain clinopyroxene with cores and dark sectors in the range Mg# 78-87 and rims and bright sectors in the range Mg# 75-84 (Fig. 4b). Þjórsárdalshraun clinopyroxenes have Mg# 76.6-84.7, while clinopyroxenes found in the nodules are more homogeneous, being in the range Mg# 83-85. Drekahraun clinopyroxene cores and dark sectors range between Mg# 81.7-85, while rims and bright sectors are in the range Mg# 79-84. Here, many reversely zoned clinopyroxenes occur with Fe-rich cores (Mg# 70-72) surrounded by Fe-poor sectors (Mg# 82-84) (Fig. 4b and 3e). Clinopyroxene dark sectors found in Veiðivötn 1477 samples vary in the range Mg# 79-85 and bright sectors in the range Mg# 75.7-82. A few clinopyroxene crystals, occurring as large single grains, are normally zoned with large Mg-rich cores of Mg# 84-85 overgrown by rims with Mg# 81-82. Reversely zoned clinopyroxenes contain Fe-rich cores (Mg# 67-75.4) followed by oscillatory zoning.

Clinopyroxene crystals can be strongly sector zoned, which is mostly reflected in their Ca, Al and Ti contents (e.g.: Nakamura, 1973; Ubide et al., 2019). In order to minimise this compositional effect, we plotted the Al_2O_3/TiO_2 vs Mg# for all clinopyroxene analyses (Fig. 4e). In general, the Al_2O_3/TiO_2 increases with increasing Mg# and the Al_2O_3/TiO_2 variation is greater for clinopyroxene with Mg# >83. Crystals with Mg# >83 show an Al_2O_3/TiO_2 span of 1.73 (1σ), in contrast to clinopyroxenes with Mg# <83 where this span is only 0.97 (1σ). Ljósufjöll and tephra cone clinopyroxenes record the largest dispersion, while recent samples have a narrower range. In fact, middle-Holocene units and historical units do sample primitive clinopyroxene in terms of Mg# and they register relatively low Al_2O_3/TiO_2 ratios and Cr_2O_3 contents. Indeed, Cr-rich (Cr_2O_3 >0.8 wt%) clinopyroxenes are exclusively sampled by the old units (Fig. S1.3c).

4.3 Olivine

In Ljósufjöll samples, unzoned olivine macrocrysts vary in composition from Fo_{84} to Fo_{87}. Zoned olivines, on the other hand, have core and rim compositions of $Fo_{82.5\text{-}87}$ and $Fo_{71\text{-}77.5}$, respectively (Fig. 4c and 3f). Olivine macrocrysts from Brandur, Fontur and Saxi have homogeneous core compositions of $Fo_{82\text{-}87.5}$ and rims between $Fo_{76\text{-}82}$ (Fig. 4c). Olivine cores from Þjórsárdalshraun and Drekahraun vary in the range $Fo_{79.5\text{-}86}$ and $Fo_{82.4\text{-}86}$, respectively. Þjórsárdalshraun olivine rims have compositions within the range $Fo_{73.6\text{-}79}$, while Drekahraun olivine rims have compositions of $Fo_{78\text{-}83}$. Reversely zoned olivines, mostly occurring in Drekahraun samples, have cores of $Fo_{66.5\text{-}82}$ encased by more primitive $Fo_{80\text{-}82}$ rims (Fig. 4c and 3f). Sparse olivines in Veiðivötn 1477 samples show a wide compositional range of cores and rims, between $Fo_{77\text{-}87}$ and $Fo_{75.4\text{-}85.5}$, respectively.

Olivine variation diagrams for all locations are shown in Fig. 4f and Fig. S1.4. Olivine cores have NiO contents between 0.1 and 0.25 wt.% that decrease to 0.05 wt.% in the rims (Fig. 4f). Fe/Mn ratio, diagnostic of parental magma compositional differences (e.g., Sobolev et al., 2007), varies between 51 and 86 (Fig. S1.4a), with more variation observed in the most primitive crystals (Fo >85, $1\sigma=5.2$) compared to olivines with Fo <85 ($1\sigma=4.3$).

4.4 Groundmass glass

Groundmass glass composition varies as a function of time (Fig. 1). From early-Holocene till present, carrier melts become more evolved. Indeed, Ljósufjöll groundmass glass is the most primitive (Fig. 1 and 5) with Mg# 57-60, MgO 7.5-9.3 wt% and TiO_2 0.95-1.1 wt%, being one of the most primitive tholeiite glass compositions known from the EVZ (see Hansen and Grönvold, 2000; Neave et al., 2014, 2017; Óladóttir et al., 2011; Passmore et al., 2012). Drekahraun and Veiðivötn 1477 groundmass glasses show a tight compositional range (Fig. 1 and 5). Drekahraun glass (Mg# 50.5-55) has MgO 7-7.5 wt% and TiO_2 1.6-1.8 wt%, whereas Veiðivötn 1477 groundmass glass

(Mg# 45.7-49.8) contains MgO 6-6.9 wt% and TiO_2 1.7-2 wt%. The groundmass of samples from Þjórsárdalshraun, assumed to represent melt compositions, refer to fine-grained pockets found in the nodules. Þjórsárdalshraun nodule glass (Fig. 2f) displays a large chemical variability (Fig. 5) (MgO 5.7-7.5 wt% and TiO_2 1.9-2.3 wt%), perhaps due to microcrystals. The compositional variation of groundmass glass from the tephra cones (B-F-S) is relatively large in comparison to other localities (Fig. 1 and 5) and our data are in good agreement with previously published data (Hansen and Grönvold, 2000). We note that Brandur generally has more primitive glass (Mg# 46-53, MgO 6.1-7.5 wt.%) than Fontur and Saxi (Mg# 40-49 and 41.5-50.5, MgO 5.5-7.5 wt% and 5.5-7 wt%, respectively).

4.5 Melt inclusions

The majority of MIs from all localities, corrected for post-entrapment processes (S1), form a group with Mg# 58-68 (Fig. 5a-d). The only locality where MI and interstitial glass compositions overlap is Ljósufjöll. Ljósufjöll MIs have MgO between 8.0-9.7 wt%, while other localities record a wider range (MgO 6.2-10.0 wt%). Among the most primitive melt inclusions (Mg# >65, MgO 8.5-10.0 wt%, n=24), two are hosted in plagioclases (An_{86-89}) from Drekahraun and Þjórsárdalshraun (MgO of MIs 8.5-8.7 wt%), one is a plagioclase-hosted (An_{90}) MI from Brandur (MgO 10.0 wt%), and the other 21 MIs are hosted in olivines ($Fo_{86.5-88}$) from the tephra cones (MgO 9.3-10.0 wt%).

Evolved MIs (Mg# <55, n=56,) are widespread in all eruptive units except Ljósufjöll. They are hosted in both plagioclase (An_{83-88}) and olivine (Fo_{76-80}). The groundmass glass and MI variations of our dataset are found to be in excellent agreement with published whole rock and glass compositions (Halldórsson et al., 2008, 2018; Hartley et al., 2018; Jakobsson, 1979; Óladóttir et al., 2011; Svavarsdóttir et al., 2017) from Bárðarbunga volcanic system (pale blue fields in Fig.

5), although our samples do not include primitive MIs with Mg# as high as 71 as found in Holuhraun samples (Bali et al., 2018; Hartley et al., 2018).

4.6 Macrocryst compositions and mineral-melt equilibrium

Figure 4a-c shows macrocryst compositional ranges, along with mineral compositions calculated to be in equilibrium with the observed groundmass glass compositions, shown with coloured bands. Equilibrium olivine compositions were calculated using a fixed Kd_{Fe-Mg}^{ol-liq} of 0.3, following Roeder and Emslie (1970), and equilibrium clinopyroxene compositions following the model of Wood and Blundy (1997). Equilibrium plagioclase compositions were calculated using equation 33 from the model of Namur et al. (2011).

Plagioclase, olivine and clinopyroxene macrocryst rims are generally found to be close to the compositions predicted to be in equilibrium with the groundmass glass, with the exception of Ljósufjöll macrocryst rims. Macrocryst cores are always too primitive to be in equilibrium with groundmass glass compositions. This feature is fairly common in mush-bearing magmas and has been observed in other eruptive units from the EVZ (Halldórsson et al., 2008, 2018; Neave et al., 2013, 2014, 2015).

5. Geothermobarometry results

5.1 Clinopyroxene storage pressures and groundmass equilibration pressures

The relative probability of clinopyroxene crystallization pressures are shown as kernel density estimates (KDE) in Fig. 6 a-d. Clinopyroxenes from all eruptive units give comparable crystallization pressure ranges of 0.5-4.5 kbar (Table 2 and Fig. 6). Each locality returns a well-defined peak in the KDE (Fig. 6a-d), located at ~2 kbar. The mean calculated pressure across all units is 2.2 ± 0.7 (1σ) kbar. Only a few clinopyroxenes (n=14, Mg#78-85) – the majority of which are from Drekahraun and the tephra cone localities – return pressures higher than 3.5 kbar. Assuming an average Icelandic crustal density of 2.86 g/cm^3 (Carlson and Herrick, 1990), our data indicate a mid-crustal magma storage zone located at 7.8 ± 2.5 (1σ) km (Fig. 6 a-d).

In Fig. 6a-d, we plot KDEs of equilibration pressures calculated for both groundmass glasses and melt inclusions. Groundmass glasses return a mean of 1.9 ± 0.8 (1σ) kbar, which is statistically indistinguishable from our calculated clinopyroxene-liquid pressures (Table 2). The majority of groundmass glasses are within the range 0.4–3.0 kbar. Similar equilibrium pressures are obtained for the Bárðarbunga Holocene tephras (Óladóttir et al., 2011a), with a mean pressure of 2.6 ± 0.4 (1σ) kbar (Fig. 6). Therefore, although the studied carrier melts have distinct and variable chemical compositions, they all last equilibrated with olivine, plagioclase and augite at essentially the same depth (Fig. 6a-d), in a mid-crustal reservoir located at 6.8 ± 2.8 (1σ) km. Barometry calculations carried out on 2014-15 Holuhraun samples reveal a magma storage zone located at about 7-8 km depths, consistent with geophysical observations (Halldórsson et al., 2018; Hartley et al., 2018).

5.2 OPAM melt inclusion equilibration pressures

Out of 436 olivine and plagioclase-hosted MIs, 299 inclusions return probability fits >0.8 (table 2 and Fig. 6a-d). The oldest, subglacial unit Ljósufjöll, records a fairly large range of MI trapping pressures, with broad peak at 3.3 kbar and a tail up to 6 kbar. Inclusions from the tephra cones display a bimodal distribution with one peak at 3.0 kbar and another at 4.9 kbar. The high-pressure peak is well defined for Brandur, Fontur and Saxi samples, with 108 MIs recording pressures higher than 4.0 kbar, but not statistically significant for Ljósufjöll inclusions due to the low number of samples (11 MIs show pressures between 4.0-6.0 kbar). Þjórsárdalshraun and Drekahraun return MI equilibration pressures in the range 0.6-4.5 kbar, with a main peak at 2.7

kbar and a minor peak at 1.9 kbar. MI in Veiðivötn 1477 samples show a bimodal distribution but the probability distribution is not well defined due to the small number of inclusions (n=28). The calculated pressures range between 1.2-4.2 kbar with a most common equilibration pressure at 3.6 kbar and a second peak at 1.8 kbar.

We have explored the relationship between MI pressures and the composition of the host crystals in all units (Fig. 7). In the subglacial unit (Fig. 7a), MIs hosted in $Fo_{\sim 86}$ olivine crystals record a most probable peak at around 2.6 kbar (9.3 km), while plagioclase-hosted MIs show a main peak at 3.9 kbar (13.9 km) and multiple secondary peaks, with the equilibration pressures up to a maximum of 6.0 kbar (21.4 km). Brandur, Fontur and Saxi cones record an even larger range of MI equilibration pressures (0.4-7.6 kbar) (Fig. 7b). Plagioclase-hosted MIs were entrapped within the pressure range 3.5-7.6 kbar (12.5-27 km) at a most probable pressure of 4.9 kbar (17.5 km). Olivine-hosted MIs were trapped at pressures within the range 0.4-7.0 kbar (1.5-25 km). MI equilibration pressures increase with the forsterite content of the host olivine, which is mainly noticeable in Fig. 7b, where we distinguish two different MI populations: (1) MIs trapped in Fo_{76-86} crystals, with a most probable pressure of 2.8 kbar (10 km) and (2) MIs hosted in Fo_{86-88} crystals, which produce the high-pressure tail of the distribution, with secondary peaks at 4.3 kbar (15.3 km) and 6 kbar (21.4 km). Macrocrysts from Brandur, Fontur and Saxi were previously studied by Hansen and Grönvold (2000). They concluded that macrophenocrysts crystallized between 7 and 40 km depth (2-11 kbar). Finally, middle-Holocene and historical units have a narrow range of MI trapping pressures (Fig. 7c), of 0.7-4.3 kbar (2.5-15 km). Olivine-hosted MIs crystallized at a most probable pressure range of 1.9-2.6 kbar (6.8-9.2 km), while plagioclase-hosted MI equilibration pressures are more variable, with a main peak at 3.3 kbar (11.7 km).

One might argue that the highest pressures calculated for the primitive melt inclusions are potentially not valid as, despite the numerical filtering, these melts might not be saturated in clinopyroxene. Using Eq. 35 of Putirka (2008), we have calculated equilibrium melt compositions for the most primitive clinopyroxene macrocrysts observed in our crystal cargo (i.e. $Mg\#_{85-87}$). We find that silicate melts with $Mg\#_{melt}$ = 61-65 are in equilibrium with Mg# 85-87 clinopyroxenes, suggesting that only inclusions with Mg#>65 should be treated with caution (n=17, circles with black thick outline in fig. 7b and 7c). Furthermore, model calculations with Petrolog (discussed in detail later) suggest that clinopyroxene with Mg# ~88 will be on the liquidus of Mg# ~65 melts at pressures of 2-6 kbar.

5.3 Geothermometry

KDEs for calculated temperatures are illustrated in Fig. 6e-h and mean temperature values are reported in Table 3. There is little variation in melt temperature between the samples, although there is some indication that the Ljósufjöll carrier melt was hotter than the carrier liquids in the other eruptions. Calculated temperatures for Ljósufjöll groundmass glass range between 1185 and 1210 °C (mean at 1193 ± 4 (1σ) °C), while samples from tephra cones, Tungnaá lava and Veiðivötn 1477 give similarly lower temperatures, with a mean at 1165 ± 7 (1σ) °C, 1170 ± 8 (1σ) °C and 1167 ± 3 (1σ) °C, respectively. Furthermore, Ljósufjöll groundmass glass temperatures are statistically indistinguishable from those derived from its melt inclusions. Across all samples, the recovered carrier melt temperatures are within the ± 26°C SEE of the thermometer (Eq. 16, Putirka, 2008), but are sufficiently different to suggest that during the last glacial period, melts erupted in the Bárðarbunga system were hotter than recent carrier magmas.

The clinopyroxene-melt thermometer returns wider temperature variations within individual samples (Fig. 6e-h), but the sample average crystallization temperatures are remarkably consistent with an overall mean crystallization temperature of 1188 ± 17 °C. We find no significant temporal variation in crystallization temperature. Finally, the plagioclase-melt and olivine-melt thermometers applied to MIs return temperatures with a narrowly focused peak at 1214 ± 10 (1σ) °C, regardless of age.

6. Discussion

6.1 Modelling fractional crystallization

The glass compositional trends in Fig. 5a-b could, to a first order, be largely controlled by fractional crystallization, although the complete variation in groundmass glass and MI major element compositions is difficult to explain solely with fractional crystallization along a single liquid line of descent. Results from our thermobarometric calculations suggest polybaric crystallisation (Fig. 6). Therefore, we calculated liquid lines of descent (LLDs) from the average composition of the most primitive melt inclusions for the whole dataset (n=24, Mg# >65) at different pressures of 0.001, 2, 4 and 6 kbar. The starting composition has Mg# of ~66, TiO_2 0.97 wt%, MgO 9.5 wt% and CaO 13.4 wt% (white stars, Fig. 5a, b). Models were run using the Petrolog3 software (Danyushevsky and Plechov, 2011), applying the pressure-sensitive mineral-melt model of Ariskin et al. (1993). Oxygen fugacity was set at the QFM buffer, assuming similar oxidation conditions to those measured in the most recent eruption of the Bárðarbunga volcano (Bali et al., 2018; Halldórsson et al., 2018).

A similar approach was used for LLDs in Fig. 5 c-d, which show Al_2O_3/TiO_2 and TiO_2/K_2O as a function of Mg#. Both diagrams show that the variability in these oxide ratios decreases with decreasing Mg#. Al_2O_3/TiO_2 in melt inclusions varies between 6 and 37 (1σ= 4.3) (Fig. 5c), while in groundmass glasses, it is between 5 and 15 (1σ= 2.1), with the Ljósufjöll carrier liquid having the highest Al_2O_3/TiO_2 (~15). A similar diversity is also observed in TiO_2/K_2O (Fig. 5d), with primitive melts recording the largest spread. Therefore, we modelled fractional crystallization at 2 kbar considering different starting compositions to encompass the observed diversity in primitive melt compositions (red stars in Fig. 5c, d). Out of the most primitive MIs (Mg# >60), we averaged MIs with high and low Al_2O_3/TiO_2, ending up with (1) a melt composition with high Al_2O_3/TiO_2 (28.1 ± 3.3 (1σ)) and (2) a melt with low Al_2O_3/TiO_2 (9.5 ± 0.4 (1σ)).

Although the trend of CaO vs. Mg# (Fig. 5a) in the glasses is roughly covered by polybaric fractional crystallisation, variation in TiO_2 (Fig. 5b) and oxide ratios such as TiO_2/K_2O (Fig. 5 c, d) cannot be explained by simple fractional crystallization of a single parental melt composition. Thus, regardless of the model and the starting composition adopted, a single LLD cannot reproduce the observed chemical variability. Therefore, we suggest that neither isobaric nor polybaric fractional crystallization alone is sufficient to describe the observed glass composition variability.

6.2 Evidence for concurrent mixing and crystallization

Element ratio variability in olivine and clinopyroxene macrocrysts and MIs provides evidence for the occurrence of diverse primary melts in the Bárðarbunga-Veiðivötn plumbing system. Clinopyroxene records a notable decrease in the variability of Al_2O_3/TiO_2 (Fig. 4e) and Cr_2O_3 (Fig. S1.3c) as clinopyroxene Mg# decreases. A similar behaviour is observed for olivine, where there is a much greater spread in Fe/Mn among Fo-rich crystals than Fo-poor crystals (Fig. S1.4a). Furthermore, we observe comparable trends in the oxide ratios of groundmass glasses and melt inclusions (e.g., Al_2O_3/TiO_2 and TiO_2/K_2O in Fig. 5c and Fig. 5d, respectively), with melt compositions at an early stage of magmatic evolution showing the greatest variability. This behaviour has been observed in samples from several Icelandic eruptions with regards to trace elements (e.g., Hartley et al., 2018; Maclennan et al., 2003; Maclennan, 2008; Neave et al., 2013).

In order to explain such variability at an early stage of magma history, we must invoke heterogeneities in the mantle source or in the melting process. As primary melts form, they start their history of magmatic evolution and progress through storage, crystallization and mixing (Maclennan, 2008). The compositional variation of primitive crystals (Fig. 4e and Fig. S1.3c) and their melt inclusions (Fig. 5c) has not been preserved with melt evolution, testifying that mixing and compositional homogenization has occurred between MI entrapment and eruption. In our samples, the most primitive MIs, hosted in olivine crystals of Fo~88, have Mg# ~67 and we do not observe olivine crystals of Fo >88. We propose that our samples do not preserve near-primary mantle-derived melts and most likely we are missing the earliest stages of the crystallization story. The most primitive melts are therefore likely to have had even more variable compositions than those preserved in our samples.

We compared our data with melt inclusion compositions from elsewhere in Iceland's EVZ. Figure 8 shows melt inclusion compositions from the 1783 AD Laki eruption (Neave et al., 2013), Skuggafjöll subglacial eruption (Neave et al., 2014), the 10 ka Grímsvötn tephra series (Neave et al., 2015) and the recent 2014-15 Holuhraun eruption (Bali et al., 2018). Naturally quenched MIs from Laki are fairly evolved with Mg# extending to much lower values (Mg# 32-60) and a very narrow range of SiO_2/TiO_2 (Fig. 8), and seem to follow a slightly different trend from our data. Conversely, melt inclusions from the 10 ka Grímsvötn (MgO up to 10.5 wt%) and Skuggafjöll (MgO up to 10.3 wt%) samples show large variations in SiO_2/TiO_2, closely matching the most primitive compositions reported in this work. Finally, melt inclusions from Holuhraun span the compositional variation recorded by our data (Fig. 8), although more primitive melts (Mg#~71), relative to our dataset, are captured by the Holuhraun melt inclusion record.

In summary, major and minor elements of macrocrysts, as well as melt inclusions, preserve evidence for compositionally diverse parental melts that might reflect heterogeneities in the mantle source or different degrees of partial melting (Maclennan, 2008). This needs to be further investigated by trace elements and stable and radiogenic isotopes. However, the compositional variability decreases as mixing and fractional crystallization progresses, producing the magma composition documented by the carrier melt.

6.3 Characteristics of the crystal cargo

In the case of Ljósufjöll macrocrysts, equilibrium with the carrier liquid is exclusively registered by plagioclase with intermediate compositions (An_{79-86}), although olivine cores are close to equilibrium (Fig. 4). We suggest that macrocrysts incorporated within the glassy groundmass are representative of the original cargo and that the macrocrysts scattered within the coarse-grained groundmass would have experienced post-emplacement crystallization of the outermost rims (An_{65-71}). The fact that Ljósufjöll samples come from a pillow lava, whose interior had longer time to cool and evolve, supports the chemical evidence for the two macrocrysts types.

In all units, macrocryst cores could not have crystallized from the respective carrier melts (Fig. 4a-c). In Fig. 9a-b, we show KDEs (coloured areas) for plagioclase and olivine macrocryst core compositions against time. We also report the most primitive mineral compositions (vertical bars), which are calculated to crystallize from the most primitive melt inclusions from each magmatic unit. Finally, we show a comparison of olivine and plagioclase macrocryst core compositions (dotted curves) in samples of subglacial (Skuggafjöll; Neave et al. 2014), early Holocene (10 ka Grímsvötn; Neave et al. 2015) and historical (1783 Laki and 2014-2015 Holuhraun eruptions; Neave et al. 2013, Halldórsson et al., 2018) eruptions that all took place in central Iceland.

Macrocryst cores are close to the predicted equilibrium compositions with melt inclusions (Fig. 9a-b), and MIs appear to be in equilibrium with plagioclase, clinopyroxene and olivine with maximum values of An ~86-87, Mg# ~85-86 (not shown) and Fo ~86-87, respectively. As a result, high-MgO melts represented by the most primitive melt inclusions could have crystallized the majority of clinopyroxene and olivine core compositions acquired in this work, although this does not apply to plagioclases with the highest An. Plagioclase macrocrysts with An>87 are widespread at all localities, and must have crystallized from melts that are not preserved in our petrological record.

Ljósufjöll has a very restricted range of plagioclase macrocryst compositions (An_{87-91}). The range of plagioclase compositions expands with time: for younger eruptive units the plagioclases are skewed towards more evolved compositions (Fig. 9a), and high-An cores are rare in the middle-Holocene and historical units. Similar relationships are observed for olivine, with the range of core compositions extending to lower Fo with time (Fig. 9b). Comparing our results with crystal compositions from the 2014-2015 Holuhraun eruption (Halldórsson et al., 2018), we find that the Holuhraun cargo records a wider distribution of plagioclase macrocryst compositions (An_{69-92}) compared to Veiðivötn 1477, but a similar distribution of olivine macrocryst compositions (Fo_{76-88}).

A similar variation of macrocryst compositions is observed when we compare available samples within the EVZ of similar age (Fig. 9a-b). We find that the subglacial Skuggafjöll (Neave et al., 2014) and 10 ka Grímsvötn (Neave et al., 2015) samples record a narrow range in plagioclase core compositions (An_{83-92}), while historical eruptions such as Laki have much more variable plagioclase compositions (An_{65-90}) (Neave et al., 2013). Interestingly, this partially also applies to olivine macrocrysts. The subglacial Skuggafjöll eruption products have a restricted olivine compositional range (Fo_{84-87}), but olivines from the 10 ka Grímsvötn show a broader and bimodal (Fo_{69-77} and Fo_{83-87}) compositional distribution. The 1783 Laki eruption has several olivine populations in the range Fo_{67-87}. However, the compositional range in Laki crystal cargo might be affected by availability of a much larger dataset compared to the other eruptions. Taken together, these data suggest that more evolved crystals have been erupted with time, both within the scale of a single volcanic system and, potentially, on the scale of the EVZ and central Iceland.

6.4 Assessing the temporal variability of the Bárðarbunga-Veiðivötn volcanic system

In the case of Iceland in the postglacial period (<12 ka), the crust has been affected by isostatic adjustments (Sigmundsson, 1991) due to ice removal and glacial rebound effects (Le Breton et al., 2016), with magma eruption rates 20-30 times higher than at present day (Maclennan et al., 2002; Sigvaldason et al., 1992). Modelling studies (Eksinchol et al., 2019; Jull and McKenzie, 1996) and chemical constraints (Eason et al., 2015; Gee et al., 1998; Hardarson and Fitton, 1991; Maclennan et al., 2002; Sinton et al., 2005; Slater et al., 1998) have provided evidence to link this eruption pulse either to the release of pooled magma enhanced by a change of the stress field in the crust (Gudmundsson, 1986; Sigvaldason et al., 1992) or to an increase in the decompression melting rate of the mantle (Jull and McKenzie, 1996; Maclennan et al., 2002) caused by the unloading of the ice cap above Iceland.

The evolution of the Bárðarbunga-Veiðivötn volcanic system in the late Pleistocene and Holocene can likely be explained within this framework and we propose three different stages (Fig. 10):

(1) A steady-state glacial stage when a 2000 m-thick ice cap (Sigmundsson, 1991) pressed down the crust, sampled by the subglacial unit (Fig. 10a). In this period the magmatic system was characterized by magma storage regions distributed over a large crustal interval of ~5-21 km (Fig. 10a). The accuracy of the OPAM barometer does not allow us to resolve the vertical arrangement of the deeper storage zones (i.e., multiple stacked sills) in the mid- to lower crust (Kelemen et al., 1997). In this period, the crystal-mush system was characterized by highly primitive macrocrysts that were picked up by a primitive and homogeneous carrier liquid.

(2) A changing state of the magmatic system, when decompression and glacial rebound effects associated with ice unloading occurred (Jull and McKenzie, 1996; Le Breton et al., 2016; Maclennan et al., 2002; Slater et al., 1998), represented by the early-Holocene tephra cones (Fig. 10b). Our results (Fig. 7) on Brandur, Fontur and Saxi samples can be interpreted as a result of an increase in magma production rates (Jull and McKenzie, 1996; Maclennan et al., 2002) that promoted the input of primitive melts from the mantle and crystallization of primitive macrocrysts in a deep-seated storage zone(s). We find that crystallization of primitive olivine ($Fo_{>85-86}$) and plagioclase ($An_{>85}$) macrocryst cores took place at a mid- to lower-crustal depths of 15-22 km (Fig. 10b). Some of these macrocrysts were transported upwards into mid-crustal reservoir(s) (7-11 km), where more evolved phases also crystallized. Furthermore, although it is still unresolved how deglaciation might have affected the chemistry of erupted melts, it is clear that early postglacial products record a greater variability in MgO contents, and are depleted in incompatible elements compared with lavas erupted when the ice load was thought to be relatively stable or absent (Eason et al., 2015; Gee et al., 1998; Jull and McKenzie, 1996; Maclennan et al., 2002; Sinton et al., 2005; Slater et al., 1998). This is consistent with our observation of a larger spread in the MgO contents of carrier liquids erupted in the early Holocene (Fig. 1).

(3) A steady-state stage, which we observe at the present, with the magmatic system being unaffected by short-term ice unloading effects, sampled by middle-Holocene and historical units (Fig. 10c). MI pressures likely indicate comparable crystallization depths of olivine and plagioclase macrocrysts in a storage zone(s) in the mid-crust. MI equilibration pressures estimated for the 2014-2015 Holuhraun eruption (Hartley et al., 2018) are all below 5 kbar (dotted KDE in fig. 7c), with the most probable pressure at 3.2 kbar (11.4 km), which is consistent with our data. We infer that since the middle-Holocene, magmas erupted in the Bárðarbunga-Veiðivötn system have

mainly carried evolved olivine and plagioclase macrocrysts (Fig. 9) that were stored at mid-crustal depths around 7-13 km (Fig. 10c).

All these clues rule out the involvement of a deep reservoir during historical eruptions, at least as a direct source for extrusives. The absence of a deep signature can be interpreted as a result of the re-establishment of a new pressure equilibrium. Shallow storage region(s) may then dominate the plumbing architecture. As seen at Etna volcano, passageways of melts in a magmatic system can change with time (Kahl et al., 2013). From this perspective, the deep reservoir(s) might be bypassed by melts coming from the mantle in historical time, most likely because new and stable magma pathway has been established. Deep earthquake swarms (~22 km) beneath the Bárðarbunga system, which have been associated with deep melt injections and melt movement (Hudson et al., 2017) are also of importance here. However, the 2014-15 Holuhraun eruption products preserve no petrologic record of crystals or melt inclusions from this depth. Our combined data suggest that since the middle-Holocene, crystals and melts from the deep storage zone have not been directly transferred to the surface. This is perhaps due to a more effective homogenisation within the mid-crustal storage zone(s). In contrast, the deep reservoir(s) was clearly sampled in the early Holocene and during subglacial eruptions, indicating that during this period the magmatic system had a different architecture that permitted direct ascent of magma from deeper storage regions to the surface.

7. Conclusions

1. Studied samples contain evidence of interaction with a crystal mush reservoir(s) and entrainment of crystal mush fragments.

2. Olivine and plagioclase macrocryst compositions vary with time. The older formations are dominated by primitive crystals, whereas in the mid-Holocene to historic formations their chemistry is skewed towards more evolved compositions.

3. Macrocryst cores and primitive melt inclusions exhibit a great chemical variability, which is likely linked to compositionally heterogeneous primary melts. The decrease of this variability, highlighted by the carrier liquid and macrocryst compositions, provides evidence for concurrent mixing and crystallization of compositionally diverse melts within the system.

4. Clinopyroxene-melt and OPAM barometries return a temporally consistent crystallization pressure of 2.2 ± 0.7 (1σ) kbar and 1.9 ± 0.8 (1σ) kbar, corresponding to a depth of 7.3 ± 2.7 (1σ) km, which are consistent with a relatively shallow reservoir located in the middle crust. These estimates are in perfect agreement with petrological and geophysical results obtained for 2014-15 Holuhraun eruption.

5. The subglacial and early-Holocene formations preserve a crystal cargo that originated from a deep reservoir with An- and Fo-rich macrocrysts crystallized at about 17.5 km (4.9 kbar) depth. In contrast, mid-Holocene to historical samples record only shallower crystallization pressures of 2-4 kbar (7-13 km). It appears that since the middle-Holocene no crystals from the deep storage zone are transferred directly to the surface, which could indicate the establishment of new magma pathways and more complete homogenization of melts in the shallow storage zone during this period.

6. At the end of the last glacial maximum, the isostatic rebound caused a significant change in the stress field of the crust and an increase in the melting rate in the upper mantle, triggering a large pulse in magmatic activity (Le Breton et al., 2016; Maclennan et al., 2002; Slater et al., 1998). Following this, during the early-Holocene, the lower crust was continuously supplied with fresh batches of melt that allowed magma from deep regions to erupt at the surface. Once crustal pressure equilibrium has been re-established following the early-Holocene, shallower storage levels dominated the system architecture with more efficient mixing and homogenisation of melts prior to eruption.

Acknowledgments

This research work was financially supported by the University of Iceland Research Fund (Nr: HI17060092) and the EIMSKIP PhD fund of the University of Iceland. We are thankful to Karl Grönvold and Maja Bar Rasmussen for collecting some of the samples. Rósa Ólafsdóttir is thanked for providing the GIS shapefiles for the geological map. We thank Matt Pankhurst and an anonymous reviewer for their valuable comments and suggestions that improved the manuscript. MH acknowledges support from NERC grant NE/P002331/1. The involvement of SAH was partly in relation to H2020 project EUROVOLC, funded by the European Commission (Grant 731070). MK acknowledges support from IRF postdoctoral fellowship grant 152726-051.

References

Ariskin, A.A., Frenkel, M.Y., Barmina, G.S., Nielsen, R.L., 1993. Comagmat: a Fortran program to model magma differentiation processes. Comput. Geosci. 19, 1155–1170. https://doi.org/10.1016/0098-3004(93)90020-6

Bali, E., Hartley, M.E., Halldórsson, S.A., Gudfinnsson, G.H., Jakobsson, S., 2018. Melt inclusion constraints on volatile systematics and degassing history of the 2014–2015 Holuhraun eruption, Iceland. Contrib. Mineral. Petrol. 173, 9. https://doi.org/10.1007/s00410-017-1435-0

Carlson, R.L., Herrick, C.N., 1990. Densities and porosities in the oceanic crust and their variations with depth and age. J. Geophys. Res. 95, 9153–9170. https://doi.org/10.1029/JB095iB06p09153

Cashman, K. V., Sparks, R.S.J., Blundy, J.D., 2017. Vertically extensive and unstable magmatic systems: A unified view of igneous processes. Science. 355, 1–9. https://doi.org/10.1126/science.aag3055

Cooper, K.M., Sims, K.W.W., Eiler, J.M., Banerjee, N., 2016. Timescales of storage and recycling of crystal mush at Krafla Volcano, Iceland. Contrib. Mineral. Petrol. 171, 1–19. https://doi.org/10.1007/s00410-016-1267-3

Danyushevsky, L. V., Plechov, P., 2011. Petrolog3: Integrated software for modeling crystallization processes. Geochem. Geophys. Geosyst. 12, 1-32. https://doi.org/10.1029/2011GC003516

Eason, D.E., Sinton, J.M., Grönvold, K., Kurz, M.D., 2015. Effects of deglaciation on the petrology and eruptive history of the Western Volcanic Zone, Iceland. Bull. Volcanol. 77, 1-27. https://doi.org/10.1007/s00445-015-0916-0

Edmonds, M., Cashman, K. V, Holness, M., Jackson, M., 2019. Architecture and dynamics of magma reservoirs. Philos. Trans. R. Soc. A. 377, 1-29

Eksinchol, I., Rudge, J.F., Maclennan, J. 2019. Rate of melt ascent beneath Iceland from the magmatic response to deglaciation. Physics.geo-ph. 1–33.

Gee, M.A.M., Taylor, R.N., Thirlwall, M.F., Murton, B.J., 1998. Glacioisostacy controls chemical and isotopic characteristics of tholeiites from the Reykjanes Peninsula, SW Iceland. Earth Planet. Sci. Lett. 164, 1–5. https://doi.org/https://doi.org/10.1016/S0012-821X(98)00246-5

Gudmundsson, A., 1986. Mechanical aspect of postglacial volcanism and tectonics of the Reykjanes Peninsula, southwest Iceland. J. Geophys. Res. 91, 12,711-12,721.

Halldórsson, S.A., Bali, E., Hartley, M.E., Neave, D.A., Peate, D.W., Guðfinnsson, G.H., Bindeman, I., Whitehouse, M.J., Riishuus, M.S., Pedersen, G.B.M., Jakobsson, S., Askew, R., Gallagher, C.R., Guðmundsdóttir, E.R., Gudnason, J., Moreland, W.M., Óskarsson, B. V, Nikkola, P., Reynolds, H.I., Schmith, J., Thordarson, T., 2018. Petrology and geochemistry of the 2014–2015 Holuhraun eruption, central Iceland: compositional and mineralogical characteristics, temporal variability and magma storage. Contrib. Mineral. Petrol. 173, 1-25. https://doi.org/10.1007/s00410-018-1487-9

Halldórsson, S.A., Oskarsson, N., Gronvold, K., Sverrisdottir, G., Steinthorsson, S., 2008. Isotopic-heterogeneity of the Thjorsa lava — Implications for mantle sources and crustal processes within the Eastern Rift Zone, Iceland. Chem. Geol. 255, 305–316. https://doi.org/10.1016/j.chemgeo.2008.06.050

Hansen, H., Grönvold, K., 2000. Plagioclase ultraphyric basalts in Iceland : the mush of the rift. J. Volcanol. Geotherm. Res. 98, 1–32.

Hardarson, B.S., Fitton, J.G., 1991. Increased mantle melting beneath Snaefellsjökull volcano during Late Pleistocene deglaciation. Nature 353, 62–64. https://doi.org/https://doi.org/10.1038/353062a0

Hartley, M.E., Bali, E., Maclennan, J., Neave, D.A., Halldórsson, S.A., 2018. Melt inclusion constraints on petrogenesis of the 2014–2015 Holuhraun eruption, Iceland. Contrib. Mineral. Petrol. 173, 1-23. https://doi.org/10.1007/s00410-017-1435-0

Hjartarson, A., 1988. Þjórsárhraunið mikla - stærsta nútímahraun jarðar (The great Þjórsá lava - The largest Holocene lava on Earth). Náttúrufræöingurinn 58, 1–16.

Holness, M.B., Anderson, A.T., Martin, V.M., Maclennan, J., Passmore, E., Schwindinger, K., 2007. Textures in partially solidified crystalline nodules: a window into the pore structure of slowly cooled mafic intrusions. J. Petrol. 48, 1243–1264. https://doi.org/10.1093/petrology/egm016

Holness, M.B., Stock, M.J., Geist, D., 2019. Magma chambers versus mush zones: constraining the architecture of sub-volcanic plumbing systems from microstructural analysis of crystalline enclaves. Philos. Trans. R. Soc. A. 377, 1-28. https://doi.org/10.1098/rsta.2018.0006

Hudson, T.S., White, R.S., Greenfield, T., Ágústsdóttir, T., Brisbourne, A., Green, R.G., 2017. Deep crustal melt plumbing of Bárðarbunga volcano, Iceland. Geophys. Res. Lett. 44, 8785–8794. https://doi.org/10.1002/2017GL074749

Jakobsson, S.P., 1979. Petrology of Recent basalts of the Eastern Volcanic Zone, Iceland. Acta Nat. Islandica 26, 1–103.

Jakobsson, S.P., Jónsson, J., Shido, F., 1978. Petrology of the western Reykjanes Peninsula, Iceland. J. Petrol. 19, 669–705. https://doi.org/10.1093/petrology/19.4.669Jull, M., McKenzie, D., 1996. The effect of deglaciation on mantle melting beneath IcelandJ. Geophys. Res. 101, 21,815-21,828.

Kahl, M., Chakraborty, S., Costa, F., Pompilio, M., Liuzzo, M., Viccaro, M., 2013. Compositionally zoned crystals and real-time degassing data reveal changes in magma transfer dynamics during the 2006 summit eruptive episodes of Mt. Etna. Bull. Volcanol. 75, 1–14. https://doi.org/10.1007/s00445-013-0692-7

Kelemen, P.B., Koga, K., Shimizu, N., 1997. Origin of gabbro sills in the Moho transition zone of the Oman ophiolite: Implications for magma transport in the oceanic lower crust. J. Geophys. Res. Solid Earth 102, 475–488. https://doi.org/10.1029/97jb02604

Langmuir, C.H., Klein, E.M., Plank, T., 1992. Petrological systematics of mid-ocean ridge basalts: constraints on melt generation beneath ocean ridges. Geophys Monograph. 71, 183–280. https://doi.org/10.1029/GM071p0183

Larsen, G., 2005. Explosive volcanism in Iceland: three examples of hydromagmatic basaltic eruptions on long volcanic fissures within the past 1200 years . Geophys. Res. Abstr. 7, 3–4.

Larsen, G., 1984. Recent volcanic history of the Veidivötn fissure swarm, southern Iceland - an approach to volcanic risk assessment. J. Volcanol. Geotherm. Res. 22, 33–58. https://doi.org/10.1016/0377-0273(84)90034-9

Larsen, G., Guðmundsson, M.T., 2014. Volcanic system : Bárðarbunga system. Cat. Icelandic Volcanoes 1–11.

Le Breton, E., Dauteuil, O., Biessy, G., 2016. Post-glacial rebound of Iceland during the Holocene. J. Geol. Soc. London 167, 417–432. https://doi.org/10.1144/0016-76492008-126.Post-glacial

Maclennan, J., 2019. Mafic tiers and transient mushes: evidence from Iceland. Philos. Trans. R.

Soc. A 377, 1-20. https://doi.org/10.1098/rsta.2018.0021

Maclennan, J., 2008. Concurrent mixing and cooling of melts under Iceland. J. Petrol. 49, 1931–1953. https://doi.org/10.1093/petrology/egn052

Maclennan, J., Jull, M., McKenzie, D., Slater, L., Grönvold, K., 2002. The link between volcanism and deglaciation in Iceland. Geochem. Geophys. Geosyst. 3, 1–25. https://doi.org/10.1029/2001GC000282

Maclennan, J., McKenzie, D., Grönvold, K., Shimizu, N., Eiler, J.M., Kitchen, N., 2003. Melt mixing and crystallization under Theistareykir, northeast Iceland. Geochem. Geophys. Geosyst. 4, 1-40. https://doi.org/10.1029/2003GC000558

Marsh, B.D., 2006. Dynamics of magmatic systems. Elements. 2, 287–292. https://doi.org/10.1016/S0074-6142(09)60100-5

McGarvie, D.W., 1984. Torfajokull: a volcano dominated by magma mixing. Geology 12, 685–688. https://doi.org/10.1130/0091-7613(1984)12<685:TAVDBM>2.0.CO;2

Mørk, M.B.E., 1984. Magma mixing in the post-glacial veidivötn fissure eruption, southeast Iceland: a microprobe study of mineral and glass variations. Lithos 17, 55–75. https://doi.org/10.1016/0024-4937(84)90006-9

Nakamura, Y., 1973. Origin of sector-zoning of igneous clinopyroxenes. Am. Mineral. 58, 986–990.

Namur, O., Charlier, B., Toplis, M.J., Vander Auwera, J., 2011. Prediction of plagioclase-melt equilibria in anhydrous silicate melts at 1-atm. Contrib. Mineral. Petrol. 163, 133–150. https://doi.org/10.1007/s00410-011-0662-z

Neave, D.A., Buisman, I., MacLennan, J., 2017a. Continuous mush disaggregation during the long-lasting Laki fissure eruption, Iceland. Am. Mineral. 102, 2007–2021. https://doi.org/10.2138/am-2017-6015CCBY

Neave, D.A., Hartley, M.E., Maclennan, J., Edmonds, M., Thordarson, T., 2017b. Volatile and light lithophile elements in high-anorthite plagioclase-hosted melt inclusions from Iceland. Geochim. Cosmochim. Acta 205, 100–118. https://doi.org/10.1016/j.gca.2017.02.009

Neave, D.A., Maclennan, J., Hartley, M.E., Edmonds, M., Thordarson, T., 2014. Crystal storage and transfer in basaltic systems: The Skuggafjoll eruption, Iceland. J. Petrol. 55, 2311_2346. https://doi.org/10.1093/petrology/egu058

Neave, D.A., Maclennan, J., Thordarson, T., Hartley, M.E., 2015. The evolution and storage of primitive melts in the Eastern Volcanic Zone of Iceland: the 10 ka Grímsvötn tephra series (i.e. the Saksunarvatn ash). Contrib. Mineral. Petrol. 170, 1–23. https://doi.org/10.1007/s00410-015-1170-3

Neave, D.A., Passmore, E., Maclennan, J., Fitton, G., Thordarson, T., 2013. Crystal-melt relationships and the record of deep mixing and crystallization in the AD 1783 Laki eruption, Iceland. J. Petrol. 54, 1661–1690. https://doi.org/10.1093/petrology/egt027

Neave, D.A., Putirka, K.D., 2017. A new clinopyroxene-liquid barometer , and implications for magma storage pressures under Icelandic rift zones. Am. Mineral. 102, 777–794. https://doi.org/http://dx.doi.org/10.2138/am-2017-5968

Óladóttir, B.A., Larsen, G., Sigmarsson, O., 2011. Holocene volcanic activity at Grímsvötn, Bárdarbunga and Kverkfjöll subglacial centres beneath Vatnajökull, Iceland. Bull. Volcanol. 73, 1187–1208. https://doi.org/10.1007/s00445-011-0461-4

Óskarsson, B. V., Andersen, C.B., Riishuus, M.S., Sørensen, E.V., Tegner, C., 2017. The mode of emplacement of Neogene flood basalts in eastern Iceland: the plagioclase ultraphyric basalts in the Grænavatn group. J. Volcanol. Geotherm. Res. 332, 26–50. https://doi.org/10.1016/j.jvolgeores.2017.01.006

Passmore, E., Maclennan, J., Fitton, G., Thordarson, T., 2012. Mush disaggregation in basaltic magma chambers: Evidence from the AD 1783 Laki eruption. J. Petrol. 53, 2593–2623.

https://doi.org/10.1093/petrology/egs061

Pedersen, G.B.M., Gudmundsson, M.T., Reynolds, H.I., Höskuldsson, A., Jónsdóttir, I., Dürig, T., Gallagher, C., Gudnason, J., Askew, R., Magnusson, E., Nikkola, P., Moreland, W.M., Drouin, V.J.P.B., Thordarson, T., Dumont, S., Óskarsson, B.V., Riishuus, M.S., Sigmundsson, F., Schmith, J., 2017. Lava field evolution and emplacement dynamics of the 2014–2015 basaltic fissure eruption at Holuhraun, Iceland. J. Volcanol. Geotherm. Res. 340, 155–169. https://doi.org/10.1016/j.jvolgeores.2017.02.027

Pinton, A., Giordano, G., Speranza, F., Thordarson, T., 2018. Paleomagnetism of Holocene lava flows from the Reykjanes Peninsula and the Tungnaá lava sequence (Iceland): implications for flow correlation and ages. Bull. Volcanol. 80, 1-19. https://doi.org/10.1007/s00445-017-1187-8

Putirka, K.D., 2008. Thermometers and Barometers for Volcanic Systems. Rev. Mineral. Geochem. 69, 61–120. https://doi.org/10.2138/rmg.2008.69.3

Roeder, P.L., Emslie, R.F., 1970. Olivine-liquid equilibrium. Contrib. Mineral. Petrol. 29, 275–289. https://doi.org/10.1007/BF00371276

Ryan, M.P., 2018. The mechanics and three-dimensional internal structure of active magmatic systems: Kilauea volcano, Hawaii. J. Geophys. Res. Solid Earth. 93, 4213–4248. https://doi.org/10.1029/JB093iB05p04213

Shorttle, O., Maclennan, J., 2011. Compositional trends of Icelandic basalts: Implications for short-length scale lithological heterogeneity in mantle plumes. Geochem. Geophys. Geosyst. 12, 1-32. https://doi.org/10.1029/2011GC003748

Sigmundsson, F., 1991. Post-glacial rebound and asthenosphere viscosity in Iceland. Geophys. Res. Lett. 18, 1131-1134.

Sigvaldason, G.E., Annertz, K., Nilsson, M., 1992. Effect of glacier loading/deloading on volcanism:

postglacial volcanic production rate of the Dyngjufjöll area, central Iceland. Bull. Volcanol. 54, 385–392. https://doi.org/10.1007/BF00312320

Sinton, J., Grönvold, K., Sæmundsson, K., 2005. Postglacial eruptive history of the Western Volcanic Zone, Iceland. Geochem. Geophys. Geosyst. 6, 1-34. https://doi.org/10.1029/2005GC001021

Sinton, J.M., Detrick, R.S., 1992. Mid-ocean ridge magma chambers. J. Geophys. Res. Solid Earth 97, 197–216. https://doi.org/10.1029/91JB02508

Slater, L., Jull, M., McKenzie, D., Gronvöld, K., 1998. Deglaciation effects on mantle melting under Iceland: results from the Northern Volcanic Zone. Earth Planet. Sci. Lett. 164, 151–164. https://doi.org/10.1016/S0012-821X(98)00200-3

Sobolev, A. V, Hofmann, A.W., Kuzmin, D. V, Yaxley, G.M., Arndt, N.T., Chung, S., Danyushevsky, L. V, Elliott, T., Frey, F. A., Garcia, M.O., Gurenko, A.A., Kamenetsky, V.S., Kerr, A.C., Krivolutskaya, N.A., Matvienkov, V. V, Nikogosian, Rocholl A., I.K., Sigurdsson, I.A., Sushchevskaya, N.M., Teklay, M., 2007. The amount of recycled crust in sources of mantle-derived melts. Science 316, 412–418. https://doi.org/10.1126/science.1138113

Svavarsdóttir, S.I., Halldórsson, S.A., Guðfinnsson, G.H., 2017. Geochemistry and petrology of Holocene lavas in the Bárðardalur region, N-Iceland. Part I: geochemical constraints on source provenance. Jökull 67, 17–42.

Thordarson, T., Höskuldsson, Á., 2008. Postglacial volcanism in Iceland. Jokull. 58, 197–228.

Thordarson, T., Larsen, G., 2007. Volcanism in Iceland in historical time: volcano types, eruption styles and eruptive history. J. Geodyn. 43, 118–152. https://doi.org/10.1016/j.jog.2006.09.005

Ubide, T., Mollo, S., Zhao, J., Nazzari, M., Scarlato, P., 2019. Sector-zoned clinopyroxene as a recorder of magma history, eruption triggers, and ascent rates. Geochim. Cosmochim. Acta.

251, 265-283. https://doi.org/10.1016/j.gca.2019.02.021

Vilmundardóttir, E.G., 1977. Tungnarhraun, jardhfraedhiskyrsla (Tungnáhraun lavas, geological report). Orkustofnun Raforkudeild 7702, 1–166.

Vilmundardóttir, E.G., Snorrason, S.P., Larsen, G., 2000. Geological map of subglacial volcanic area southwest of Vatnajökull icecap, Iceland, 1: 50.000. Natl. Energy Auth. Natl. Power Company, Reykjavík, Iceland.

West, M., Menke, W., Tolstoy, M., Webb, S., Sohn, R., 2001. Magma storage beneath axial volcano on the Juan de Fuca mid-ocean ridge. Nature 413, 833-836.

Wood, B.J., Blundy, J.D., 1997. A predictive model for rare earth element partitioning between clinopyroxene and anhydrous silicate melt. Contrib. Mineral. Petrol. 129, 166–181. https://doi.org/10.1007/s004100050330

Yang, H.-J., Kinzler, R.J., Grove, T.L., 1996. Experiments and models of anhydrous, basaltic olivine-plagioclase-augite saturated melts from 0.001 to 10 kbar. Contrib. Mineral. Petrol. 124, 1–18. https://doi.org/10.1007/s004100050169

Zellmer, G.F., Rubin, K.H., Gronvöld, K., Jurado-Chichay, Z., 2008. On the recent bimodal magmatic processes and their rates in the Torfajökull–Veidivötn area, Iceland. Earth Planet. Sci. Lett. 269, 388–398. https://doi.org/10.1016/j.epsl.2008.02.026

Figure captions

Fig. 1. Temporal variation of MgO content in glasses from the Bárðarbunga-Veiðivötn volcanic system. Subglacial (Ljósufjöll), early-Holocene (Brandur, Fontur and Saxi tephra cones), middle-Holocene (Drekahraun) and Veiðivötn 1477 data are presented in this study. 'Holocene Bárðarbunga' glass compilation from Óladóttir et al. (2011). 2014-2015 Holuhraun eruption glass composition from Halldórsson et al. (2018). Temporal evolution trends are also observed in CaO, FeO and TiO_2 contents (not shown).

Fig. 2. Geological map of the southernmost part of the Bárðarbunga-Veiðivötn system. The general geology of the area is indicated with greyscale colours. Eruptive units studied in this work are marked in colours. Historic lavas are younger than 1100 BP; prehistoric lavas are older than 1100 BP. Triangles show the exact sampling location within each unit. The insert map in the upper left corner shows the outline of the active neovolcanic zones (in grey) and the Bárðarbunga-Veiðivötn system (BV) in red. RR: Reykjanes Ridge; RVB: Reykjanes Volcanic Belt; SVB: Snæfellsnes Volcanic Belt; WVZ: Western Volcanic Zone; MIB: Mid-Iceland Belt; BV: Bárðarbunga-Veiðivötn system; EVZ: Eastern Volcanic Zone; OVB: Öraefajökull Volcanic Belt; NVZ: Northern Volcanic Zone. Geological map compiled by Haukur Jóhannesson and Kristján Sæmundsson published by the Icelandic Museum of Natural History and Iceland Geodetic Survey.

Fig. 3. Backscattered electron (BSE) images showing the main petrographic and chemical features of the studied samples. a) Plagioclase macrocryst from the Veiðivötn 1477 eruption with an oscillatory zoned interior surrounded by a darker rim. b) Glomerophyric clot from Drekahraun. Sector zoned clinopyroxene crystals that have grown with plagioclases. c) Clinopyroxene macrocryst from Veiðivötn 1477 showing resorbed dark cores enclosed by less primitive rims. d) Normally zoned olivine with a large melt inclusion from Brandur. e) Saxi tephra cone nodule with olivine and plagioclase macrocrysts and clinopyroxene in glomerophyric clots. f) Nodule from Þjórsárdalshraun: plagioclase crystals surrounded by homogeneous clinopyroxene; interstitial glass pockets are also observed. g) Plagioclase crystal from Ljósufjöll with crystalline melt inclusions, surrounded by a coarse-grained groundmass. h) Plagioclase crystal from Ljósufjöll within a glassy groundmass. plg= plagioclase; ol= olivine; cpx= clinopyroxene; mi= melt inclusion; gl= interstitial glass; Fo=olivine fosterite content; An=plagioclase anorthite content; Mg#= clinopyroxene Mg#.

Fig. 4. The range in (a) An content of plagioclase, (b) Mg# of clinopyroxene, and (c) Fo content of olivine for each locality. Core and rim compositions are depicted as circles and diamonds, respectively. Clinopyroxene dark and bright sectors refer to sector zones in BSE images. Coloured bands represent the mineral compositions calculated to be in equilibrium with the carrier liquid for each sample, where the glass composition is taken as representative of the carrier melt. Numbers in each corner state the number of point analyses in minerals for that specific locality and mineral phase. In general, macrocryst cores are more primitive than the equilibrium compositions whilst rims are more evolved and tend to overlie the equilibrium bands. Lj: Ljósufjöll; B: Brandur; F: Fontur; S: Saxi; Th: Þjórsárdalshraun; Dr: Drekahraun; V: Veiðivötn 1477. (d)-(f) Variation diagrams showing the TiO_2 content vs An content of plagioclase (d), Al_2O_3/TiO_2 vs Mg# clinopyroxene (e), and NiO content vs Fo content of olivine (f) macrocrysts. 1σ error is smaller than the symbol sizes unless otherwise shown.

Fig. 5. Variation diagrams showing (a) CaO content, (b) TiO_2 content, (c) Al_2O_3/TiO_2, and (d) TiO_2/K_2O vs Mg# of groundmass glasses (circles) and melt inclusions (triangles) from the studied samples. Liquid lines of descent (LLD) in (a) and (b) are calculated starting from the same melt composition (white stars) at different pressures. LLDs in (c) and (d) are calculated at 2 kbar, using two different starting compositions (red stars). See main text for details. All LLDs were calculated using Petrolog3 (Danyushevsky and Plechov, 2011). Blue fields denote published data from Bárðarbunga-Veiðivötn system (Halldórsson et al., 2008, 2018; Hartley et al., 2018; Jakobsson, 1979; Óladóttir et al., 2011; Svavarsdóttir et al., 2017). Low K_2O data within the ellipse were acquired from glassy to cryptocrystalline areas which could be affected by quench modifications. 1σ error is smaller than the symbols.

Fig. 6. Kernel density estimate plots, with bandwidth 0.3, of calculated pressures (a)-(d) and temperatures (e)-(h) for all studied units. Clinopyroxene-melt pressures are calculated using the Neave and Putirka (2017) barometer; OPAM barometry (Hartley et al., 2018; Yang et al., 1996) was applied both to glasses and PEC-corrected melt inclusions. Reported MI pressures represent compositions with a returned probability of fit higher than 80%. Temperatures are calculated using a glass-only thermometer and cpx, ol and plag-melt thermometers from Putirka (2008). See the main text for more details. The dotted curve in each plot shows the pressure and temperature distribution for Holocene Bárðarbunga glasses from Óladóttir et al. (2011). Errors (± next to the

legend) indicate the standard error of estimate of the thermometers and barometers used. Table 2 lists the numbers of processed cpx, glass and MIs for each locality.

Fig. 7. Relationship between host mineral composition and melt inclusion equilibration pressure, for (a) subglacial unit (Ljósufjöll) (b) early-Holocene units (Brandur, Fontur and Saxi cones) and (c) middle-Holocene/historical units (Tungnaá lavas and Veiðivötn 1477). Kernel density estimates to the right of the plots show the relative probability of equilibration pressures for olivine- and plagioclase-hosted melt inclusions. MI pressure distributions for Holohraun eruption is reported as dotted curve. Error bars refer to the OPAM standard error of estimate (SEE=1.3 kbar). MIs outlined with dotted lines have Mg#>65 and are the least likely to be three-phase saturated.

Fig. 8. SiO_2/TiO_2 vs Mg# of melt inclusions from this work along with published data from the subglacial Skuggafjöll eruption (Neave et al., 2014), the 10 ka early-Holocene Grímsvötn eruption (Neave et al., 2015), the historical 1783 Laki eruption (Neave et al., 2013) and the 2014-15 Holuhraun eruption (Bali et al., 2018). Our melt inclusions span the compositional variability recorded by other eruptions form the EVZ. Also indicated are depleted and enriched end-member melt compositions for the Northern Volcanic Zone (NVZ, red stars) and the Western Volcanic Zone (WVZ, white stars) (Shorttle and Maclennan, 2011). 1σ error is within the symbol sizes.

Fig. 9. Kernel density estimate (KDE) curves showing the relative probability of plagioclase and olivine compositions and how the probability has changed with time (a) An content of plagioclase macrocryst cores (b) Fo content of olivine macrocryst cores. Coloured bars indicate the mineral composition in equilibrium with the most primitive MIs within each magmatic unit. Dotted and dashed lines show KDE for published subglacial and Holocene eruption data for the EVZ. Skuggafjöll (Neave et al., 2014); 10ka Grímsvötn (Neave et al., 2015); 1783 Laki (Neave et al., 2013); 2014-2015 Holuhraun (Halldórsson et al., 2018).

Fig. 10. Schematic cartoon summarizing the proposed evolution of the Bárðarbunga-Veiðivötn magmatic system over time, based on barometry, thermometry and chemical data. a) Subglacial time. The magmatic system is distributed over a wide range of depths, with a main storage zone in the middle crust. At that time, crystal mush bodies were mostly composed of primitive macrocrysts. b) Early-Holocene time when the magmatic system underwent glacial

rebound effects. The magmatic system is characterized by (1) a storage zone in the mid-crust at around 10 km depth, mostly made up of evolved macrocrysts and (2) a deep-crustal zone(s) at 17 km depth, where more primitive macrocrysts crystallize. The increase in magma productivity facilitated movement of magma from deep regions to the surface. c) The magmatic system configuration since the middle-Holocene. The magmatic system is most likely dominated by a mid-crustal reservoir, with crystal mush horizon(s) made up of evolved macrocrysts. Once crustal pressure equilibrium has been established, mid-crustal storage zone(s) dominate the magmatic system configuration, with new magma passageways being established and melts being homogenized in the middle crust. Primitive plagioclase and olivine crystals are coloured in grey and dark green respectively; evolved plagioclase and olivine crystals are coloured in white and light green respectively. Bár: Bárðarbunga edifice; Veið: Veiðivötn area; plg: plagioclase; ol: olivine; cpx: clinopyroxene; dsl: deactivated/disconnected storage levels; xx=crystal.

Figure 1

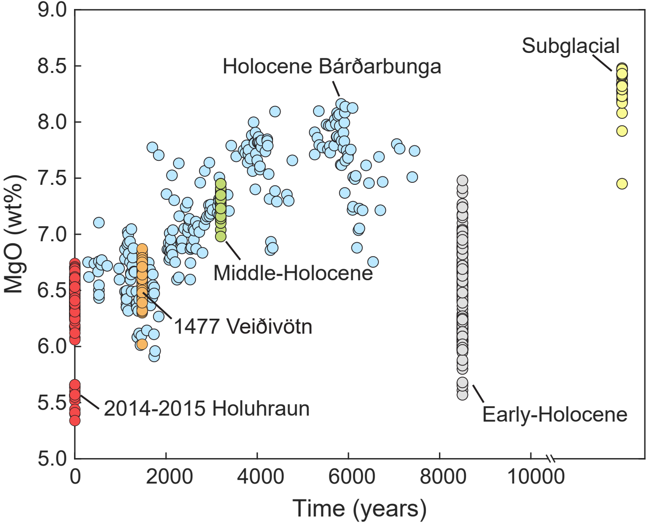

9.0
8.5
8.0
7.5
7.0
6.5
6.0
5.5
5.0
MgO (wt%)
0
2000
4000
6000
8000
10000
Time (years)
Subglacial
Holocene Bárðarbunga
Middle-Holocene
1477 Veiðivötn
2014-2015 Holuhraun
Early-Holocene

Figure 2

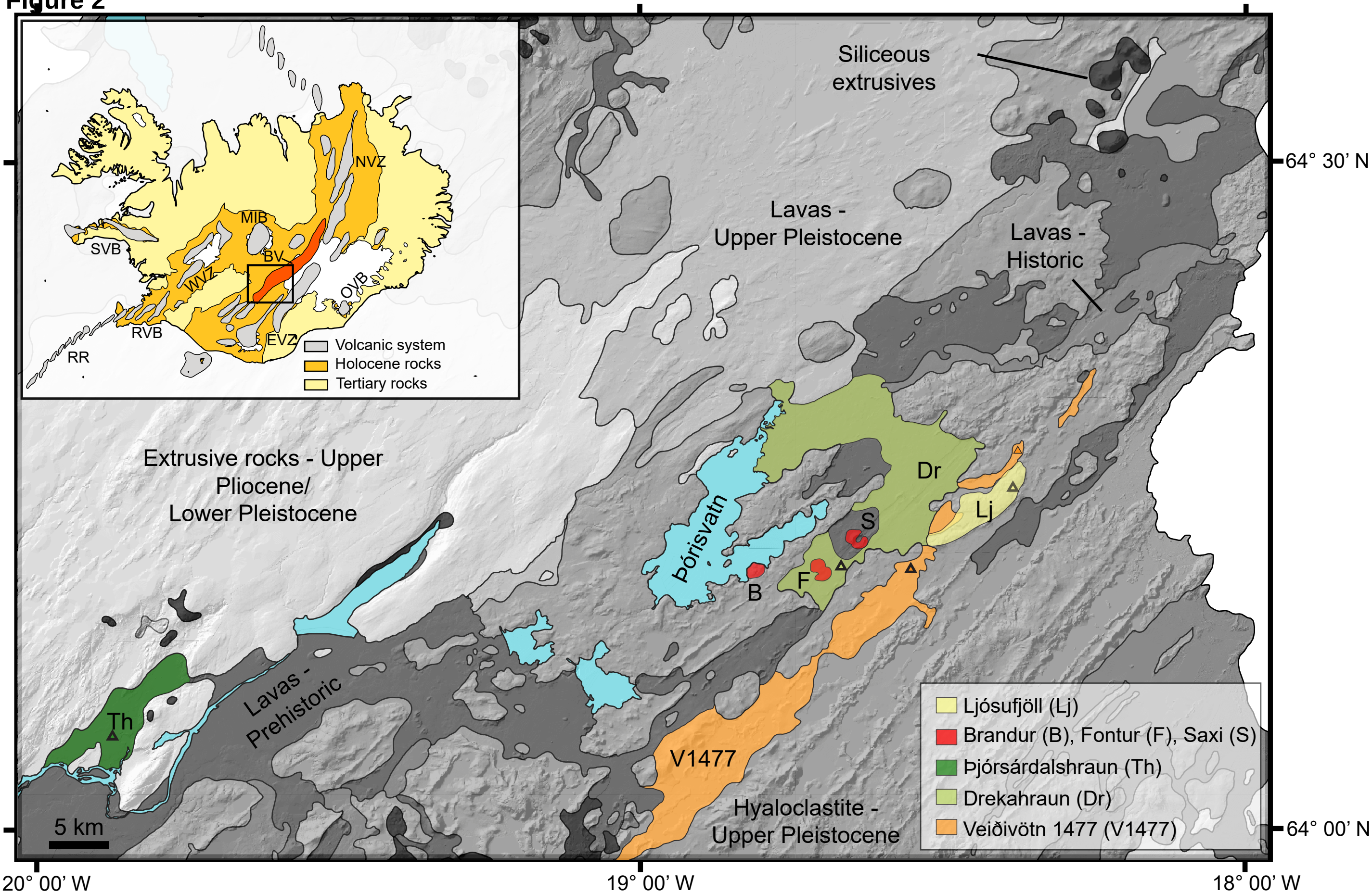

NVZ
MIB
BV
SVB
WVZ
OVB
RVB
EVZ
RR
Volcanic system
Holocene rocks
Tertiary rocks
Siliceous extrusives
Lavas - Upper Pleistocene
Lavas - Historic
64° 30' N
Extrusive rocks - Upper Pliocene/ Lower Pleistocene
Þórisvatn
Dr
Lj
S
B
F
Th
Lavas - Prehistoric
V1477
Hyaloclastite - Upper Pleistocene
5 km
Ljósufjöll (Lj)
Brandur (B), Fontur (F), Saxi (S)
Þjórsárdalshraun (Th)
Drekahraun (Dr)
Veiðivötn 1477 (V1477)
64° 00' N
20° 00' W
19° 00' W
18° 00' W

Figure 3

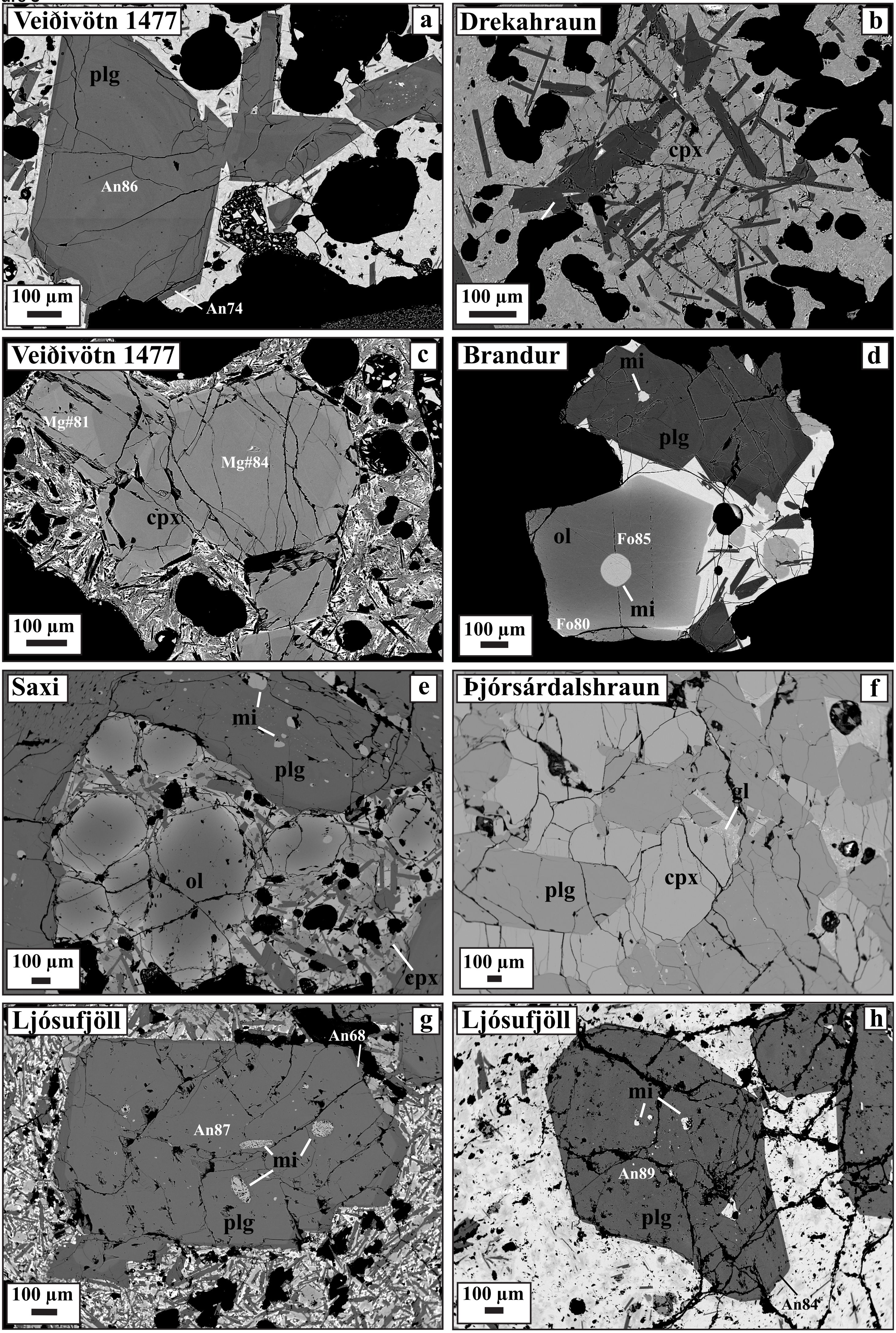

Veiðivötn 1477
a
plg
An86
An74
100 µm
Drekahraun
b
cpx
100 µm
Veiðivötn 1477
c
Mg#81
Mg#84
cpx
100 µm
Brandur
d
mi
plg
ol
Fo85
mi
Fo80
100 µm
Saxi
e
mi
plg
ol
cpx
100 µm
Þjórsárdalshraun
f
gl
cpx
plg
100 µm
Ljósufjöll
g
An68
An87
mi
plg
100 µm
Ljósufjöll
h
mi
An89
plg
An84
100 µm

Figure 4

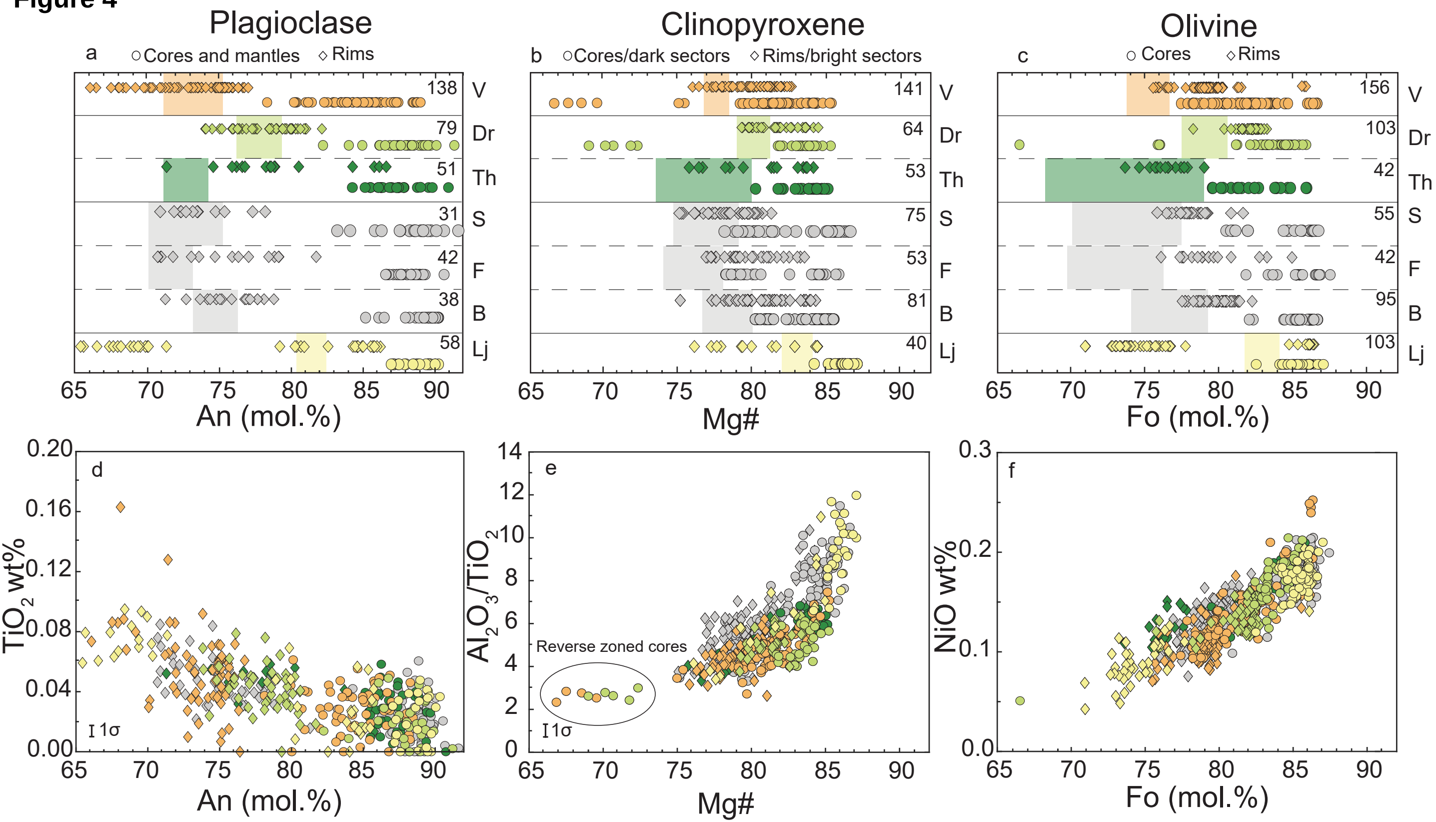

Plagioclase
Clinopyroxene
Olivine
a
Cores and mantles
Rims
b
Cores/dark sectors
Rims/bright sectors
c
Cores
Rims
V
Dr
Th
S
F
B
Lj
138
79
51
31
42
38
58
141
64
53
75
53
81
40
156
103
42
55
42
95
103
An (mol.%)
Mg#
Fo (mol.%)
d
e
f
TiO2 wt%
Al2O3/TiO2
NiO wt%
Reverse zoned cores
1σ

Figure 5

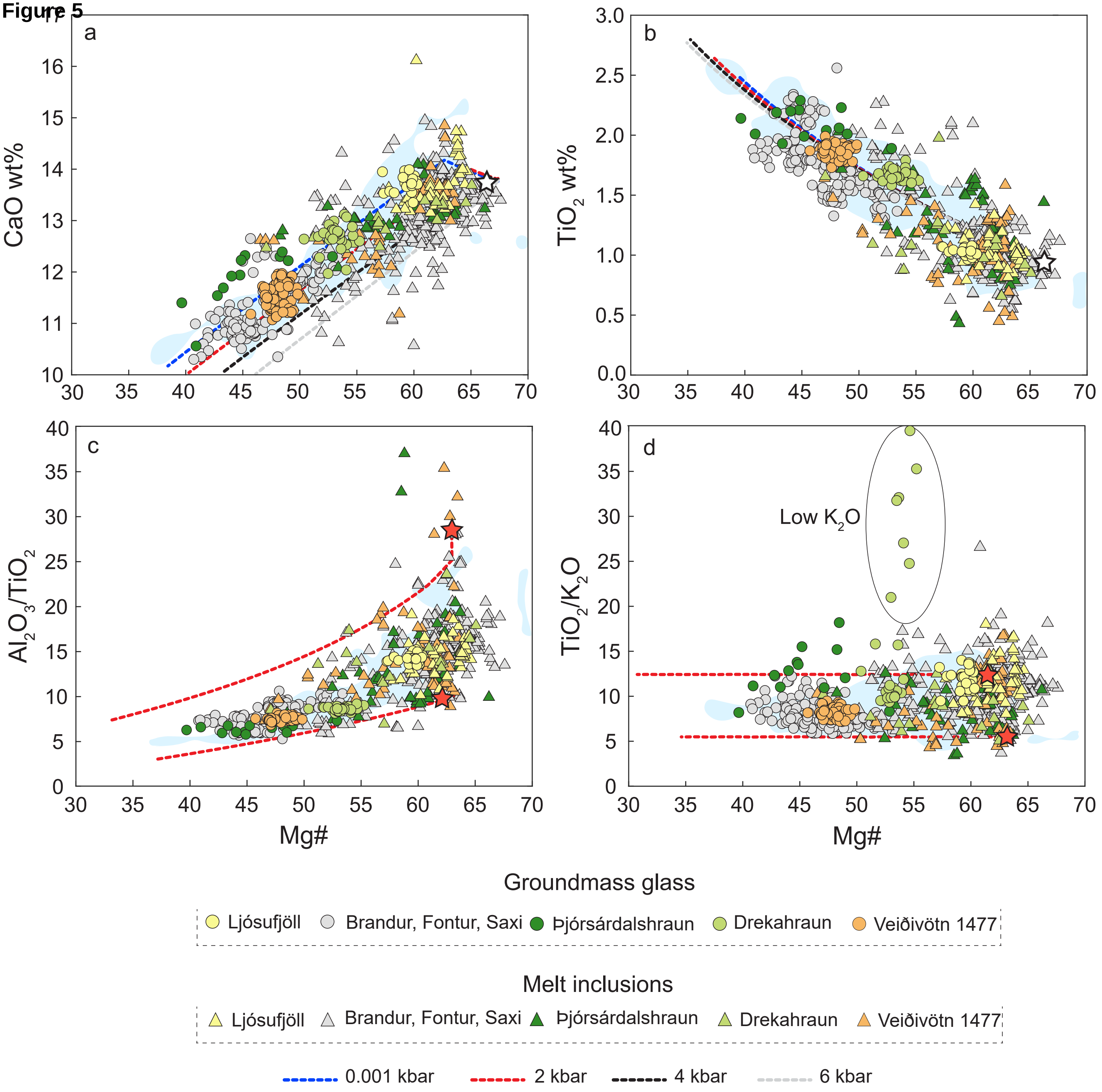

a
CaO wt%
b
TiO2 wt%
c
Al2O3/TiO2
d
TiO2/K2O
Low K2O
Mg#
Mg#
Groundmass glass
Ljósufjöll
Brandur, Fontur, Saxi
Þjórsárdalshraun
Drekahraun
Veiðivötn 1477
Melt inclusions
Ljósufjöll
Brandur, Fontur, Saxi
Þjórsárdalshraun
Drekahraun
Veiðivötn 1477
0.001 kbar
2 kbar
4 kbar
6 kbar

Figure 6

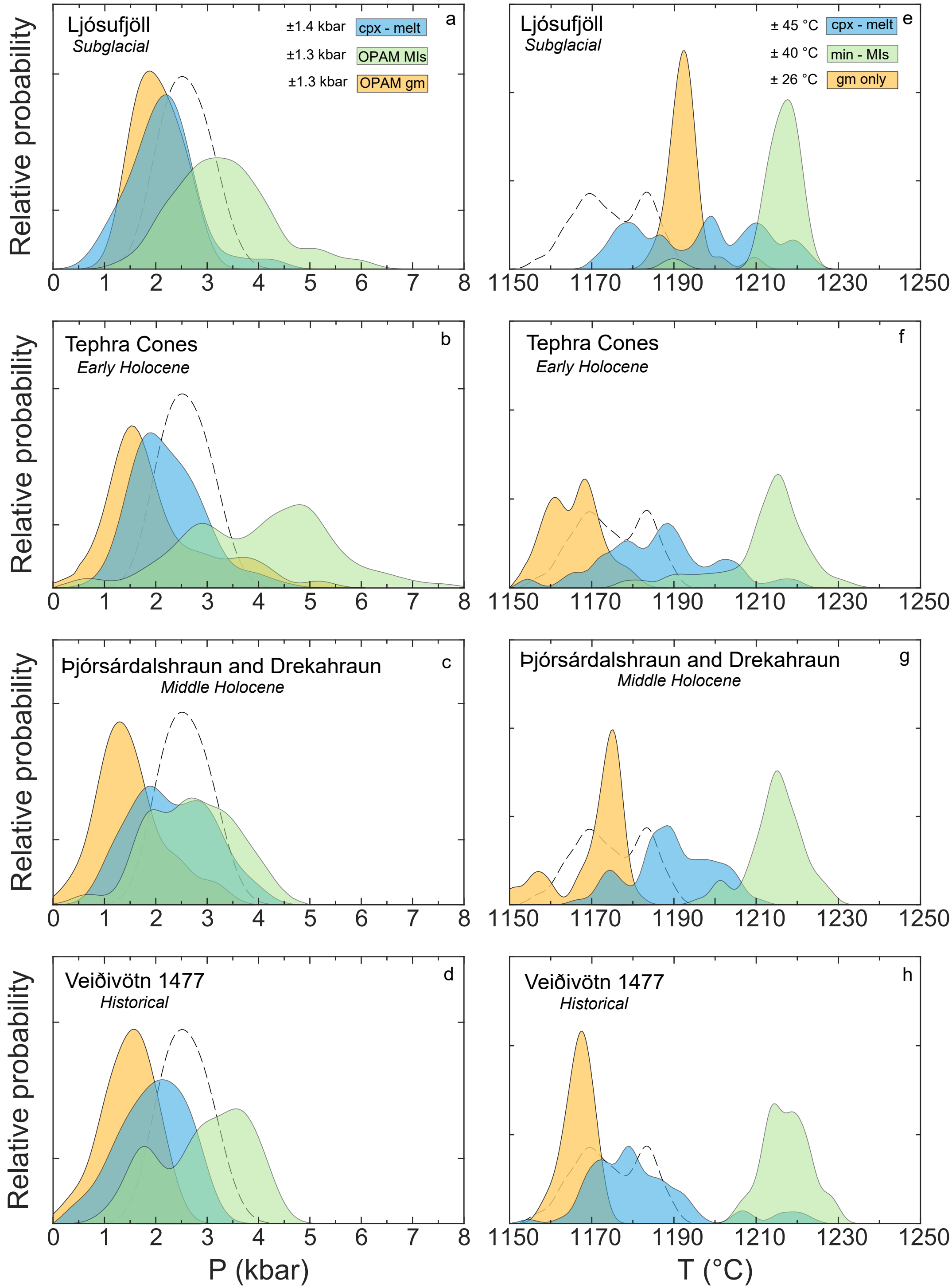
Ljósufjöll
Subglacial
±1.4 kbar
cpx - melt
±1.3 kbar
OPAM MIs
±1.3 kbar
OPAM gm
a
Tephra Cones
Early Holocene
b
Þjórsárdalshraun and Drekahraun
Middle Holocene
c
Veiðivötn 1477
Historical
d
Relative probability
P (kbar)
Ljósufjöll
Subglacial
± 45 °C
cpx - melt
± 40 °C
min - MIs
± 26 °C
gm only
e
Tephra Cones
Early Holocene
f
Þjórsárdalshraun and Drekahraun
Middle Holocene
g
Veiðivötn 1477
Historical
h
T (°C)

Figure 7

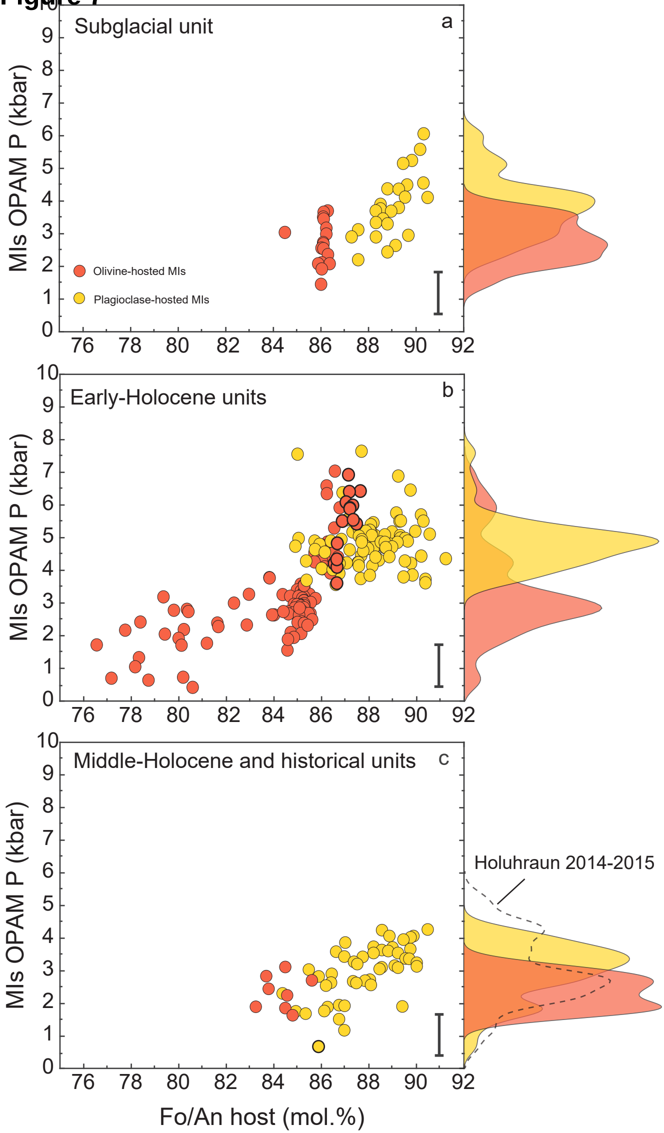

Subglacial unit
a
Olivine-hosted MIs
Plagioclase-hosted MIs
Early-Holocene units
b
Middle-Holocene and historical units
c
Holuhraun 2014-2015
MIs OPAM P (kbar)
Fo/An host (mol.%)
0
1
2
3
4
5
6
7
8
9
10
76
78
80
82
84
86
88
90
92

Figure 8

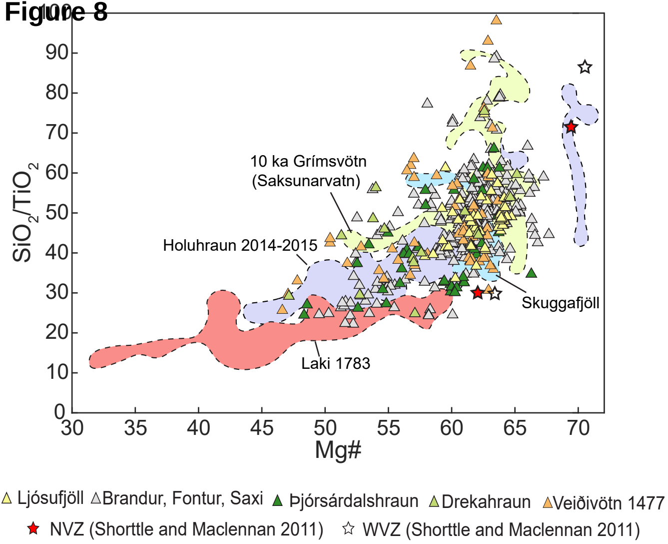
100
90
80
70
60
50
40
30
20
10
0
30
35
40
45
50
55
60
65
70
Mg#
SiO2/TiO2
10 ka Grímsvötn
(Saksunarvatn)
Holuhraun 2014-2015
Skuggafjöll
Laki 1783
Ljósufjöll
Brandur, Fontur, Saxi
Þjórsárdalshraun
Drekahraun
Veiðivötn 1477
NVZ (Shorttle and Maclennan 2011)
WVZ (Shorttle and Maclennan 2011)

Figure 9

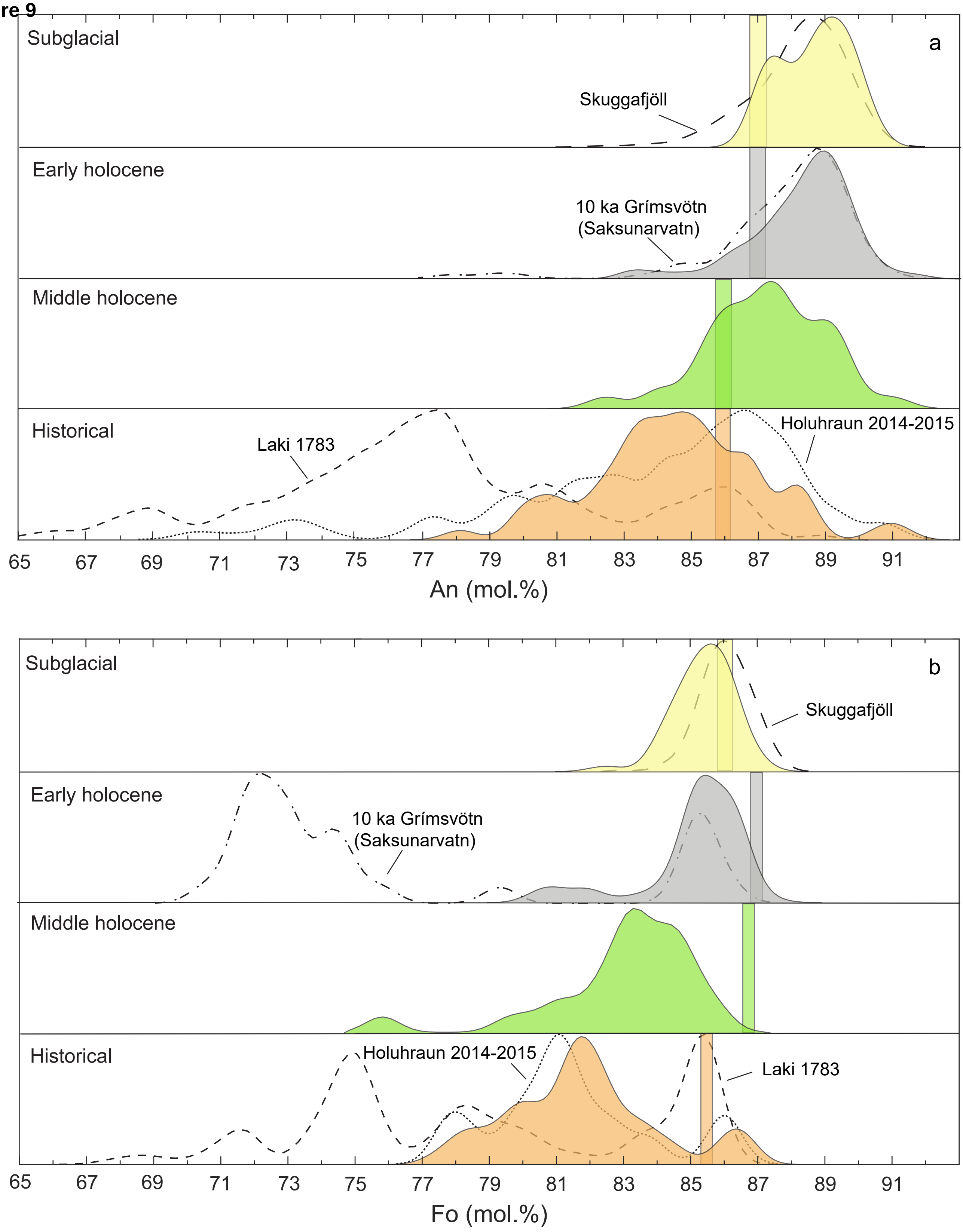

Subglacial
a
Skuggafjöll
Early holocene
10 ka Grímsvötn
(Saksunarvatn)
Middle holocene
Historical
Laki 1783
Holuhraun 2014-2015
65
67
69
71
73
75
77
79
81
83
85
87
89
91
An (mol.%)
Subglacial
b
Skuggafjöll
Early holocene
10 ka Grímsvötn
(Saksunarvatn)
Middle holocene
Historical
Holuhraun 2014-2015
Laki 1783
65
67
69
71
73
75
77
79
81
83
85
87
89
91
Fo (mol.%)

Figure 10

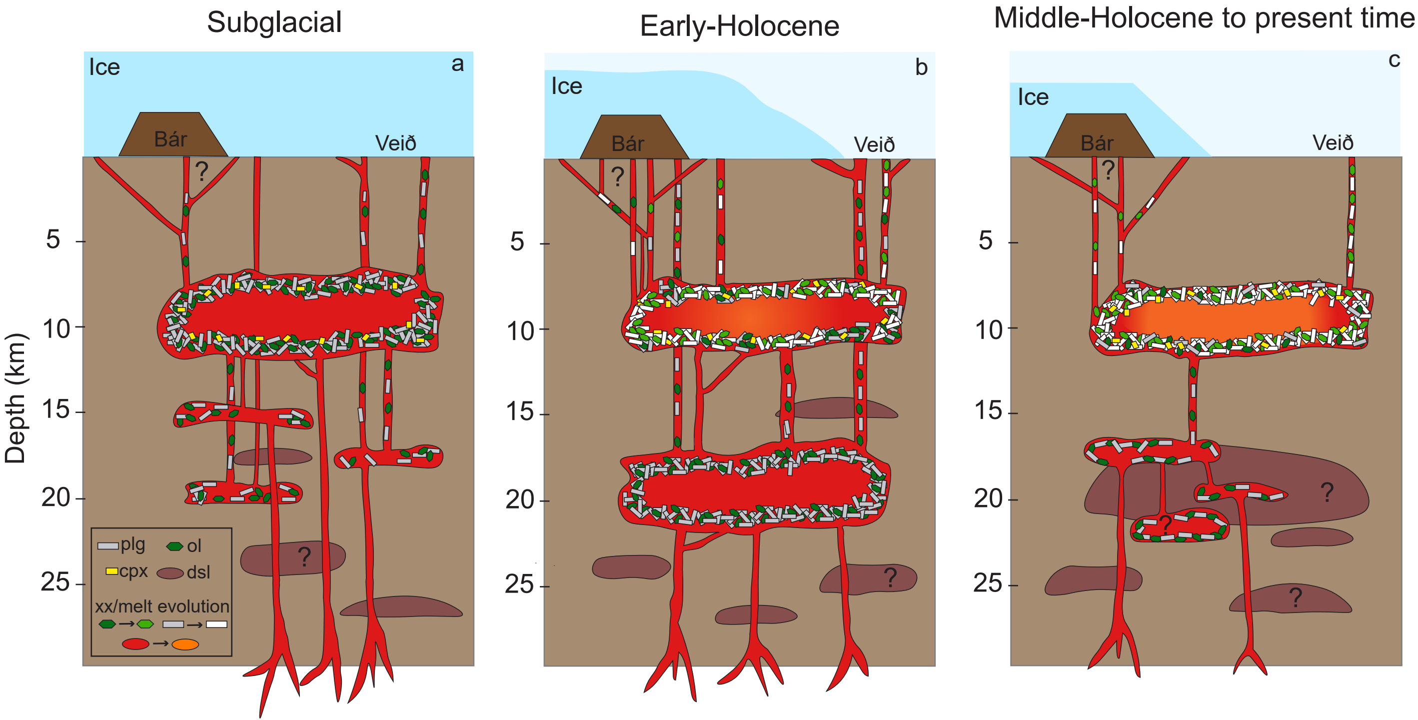

Subglacial
Early-Holocene
Middle-Holocene to present time
Ice
a
b
c
Bár
Veið
?
Depth (km)
5
10
15
20
25
plg
ol
cpx
dsl
xx/melt evolution

Table 1
Click here to download Table: Table 1.docx

Table 1. Sample list, description and location.

Sample name	Age	Coordinates		Description	Previous work
		Latitude (N)	Longitude (W)		
Ljósufjöll	Subglacial	64° 16' 51.2''	18° 23' 40.8''	pillow lava	-
Brandur	Early Holocene	64° 13' 55.6''	18° 48' 8.6''	lava, tephra, nodules	Hansen and Grönvold (2000), Holness et al. (2007)
Fontur	Early Holocene	64° 15' 17.9''	18° 38' 0.2''	lava, tephra, nodules	Hansen and Grönvold (2000), Halldorsson et al. (2008), Holness et al. (2007)
Saxi	Early Holocene	64° 13' 49.2''	18° 42' 15.7''	lava, tephra, nodules	Hansen and Grönvold (2000), Halldorsson et al. (2008), Holness et al. (2007)
Þjórsárdalshraun	Middle-Holocene	64° 08' 43.2''	19° 49' 26.8''	lava with nodules	-
Drekahraun	Middle-Holocene	64° 14' 0.4''	18° 39' 57.2''	fresh scoria	-
Veiðivötn 1477	Historical (1477 AD)	64° 14' 29.2''	18° 31' 50.7''	fresh scoria	-

Table 2
Click here to download Table: Table 2.docx

Table 2. Number of clinopyroxenes, groundmass glasses and MIs processed for geobarometry estimates along with pressure results. Pressures are in kbar.

	cpx-melt barometry				OPAM barometry									
	Clinopyroxenes				Groundmass glasses				Melt inclusions					
	n. analysis	n. cpx-melt	P		n. analysis	P_f>80%	P		n. analysis		P_f>80%		P	
			Mean	σ			Mean	σ	ol-hosted	plg-hosted	ol-hosted	plg-hosted	Mean	σ
Ljósufjöll	43	40	2.1	0.6	29	26	2.0	0.4	18	30	17	24	3.3	0.9
Brandur	59	45	2.2	0.7	69	42	1.6	0.6	86	37	73	22	3.6	1.5
Fontur	34	24	2.2	0.6	33	6	3.5	0.9	24	54	20	31	4.4	1.1
Saxi	47	35	2.3	0.7	63	5	3.2	1.5	39	37	17	33	4.4	1.3
Þjórsárdalshraun	41	35	1.9	0.7	13	11	1.5	0.8	5	33	5	23	2.7	0.9
Drekahraun	63	45	2.6	0.8	30	6	1.5	0.2	0	17	0	6	2.9	1.0
Veiðivötn 1477	144	90	1.9	0.6	91	15	1.5	0.5	4	52	3	25	2.9	0.9
Total	431	314			328	111			176	260	135	164		

P_f = probability of fit ; σ= standard deviation

Table 3
Click here to download Table: Table 3.docx

Table 3. Mean temperature (°C) values along with the standard deviation (σ) for all studied localities.

	Groundmass glasses			Melt inclusions			Cpx - melt		
	n	Mean	σ	n	Mean	σ	n	Mean	σ
Ljósufjöll	29	1193	4	48	1216	6	40	1197	15
Brandur	69	1170	4	123	1213	9	45	1194	22
Fontur	33	1161	7	78	1213	8	24	1186	12
Saxi	63	1163	5	76	1209	16	35	1186	20
Þjórsárdalshraun	13	1160	9	42	1214	7	35	1187	10
Drekahraun	30	1174	2	17	1216	5	45	1188	15
Veiðivötn 1477	91	1167	3	56	1217	5	90	1182	14